FABRICATION OF CZTS AND ZnO NANO-RODS FOR SOLAR CELL APPLICATION

CHAN HEUNG TANG

M.Phil

The Hong Kong Polytechnic University

2014

THE HONG KONG POLYTECHNIC UNIVERSITY

DEPARTMENT OF APPLIED PHYSICS

FABRICATION OF CZTS AND ZnO NANO-RODS FOR SOLAR CELL APPLICATION

CHAN HEUNG TANG

A thesis submitted in partial fulfillment of the requirements for the degree of Master of Philosophy

August 2013

CERTIFICATE OF ORIGINALITY

I hereby declare that this thesis is my own work and that, to the best of my knowledge and belief, it reproduces no material previously published or written, nor material that has been accepted for the award of any other degree or diploma, except where due acknowledgement has been made in the text.

_____ (Signed)

_____Chan Heung Tang_____ (Name of student)

Abstract

Transparent zinc oxide (ZnO) films had been grown on indium tin oxide (ITO) glass using potentiostatic cathodic deposition technique. Aqueous zinc nitrate was used as electrolyte. In this project, different deposition parameters such as applied cathodic potential, and concentration of electrolyte had been used to fabricate the ZnO films. Their structural and optical properties were characterized by X-ray diffractometer (XRD), scanning electron microscope (SEM), diffuse reflectance UV-VIS spectrophotometer and photoluminescence (PL) spectrometer. The band gap of the ZnO was determined using the emission curve of photoluminescence which is about 3.3eV. On the basis of our measurements, the effects of different deposition parameters on the structural and optical properties of the ZnO films have been investigated.

Cu_2ZnSnS_4 (CZTS) nanoparticles with sizes of 5–15 nm were successfully synthesized using hydrothermal process at a relatively low temperature of 130°C. Non-toxic and inexpensive precursors including copper chloride, zinc chloride, thiourea and oleyamine were used. The effects of the key processing parameters, such as hydrothermal temperature and composition ratio of the precursors, on the structural properties of CZTS were investigated. The higher the reaction temperature within the range between 130°C and 180°C the better the crystallinity of CZTS was. In order to obtain stoichiometric CZTS, the amount of Zn and S used were far more than they supposed to be used i.e. Cu:Zn:Sn:S=2:5:1:9. CZTS nanoparticles were then dispersed into toluene to form suspending solution which was deposited on ITO-coated glass

substrates using dip-coating method. The structural properties of CZTS particle films were characterized with X-ray Diffraction (XRD), Scanning Electron Microscope (SEM), and Transmission Electron Microscopy (TEM) and Raman spectroscopy. The band gap of the CZTS was determined using the emission curve of photoluminescence.

Based on the ZnO films and CZTS nanoparticles, solar structures were developed. Different kinds of solution were used to disperse the CZTS nanoparticles on top of ZnO/ITO films. After successfully dispersion of the CZTS, Molybdenum was used as the top electrode. Finally, the result of this photovoltaic device was measured by solar stimulator.

Acknowledgements

This research has been carried out for the past two years in The Hong Kong Polytechnic University. I would like to acknowledge many people who have given helps and guidance to me, especially my supervisor, Dr. C. L. Mak for his continuous encouragement, support and guidance during this study.

I would also like to thank the technical support provided by the Materials Research Centre (MRC) and all the staff members in the Department of Applied Physics of The Hong Kong Polytechnic University. The financial support for the author's graduate studies from the Research Committee of The Hong Kong Polytechnic University is acknowledged.

Finally, I would like to acknowledge the supports and helps from my family and my friends during this study.

Table of contents

List of figures and tables

Chapter 1 Introduction

1.1 Introduction

Global warming has become the most controversial issue of the past decade. Over the past century, the average temperature of Earth has risen 0.78 ^{o}C**.** Scientists from the United States Environmental Protection Agency forecast another 2 ^{o}C - 6 ^{o}C increment in the following decades. Global warming has been used to describe the continuous temperature increment in the Earth surface which can be mainly attributed to drastically increased ejection of greenhouse gases to the atmosphere. Greenhouse gas refers to gas that can trap the energy from sun to Earth and obstacle heat release to the universe. Gases such as Carbon dioxide (CO_2), Methane (CH_4), Nitrous oxide (N_2O) and Flourinated gases are known as greenhouse gas [1]. Global warming is an obvious aspect of climate change. Furthermore it also leads to many other different climates crisis. Even a tiny change in the Earth's average temperature will lead to dangerous shifting in climate and weathering. Many evidences show that weather and climate changes are always correlated to temperature changes in the atmosphere [2] [3]. Drought, flooding, heat waves and intensive rains are of more severe and frequent in different places. Besides, the global warming also causes melting of ice caps; ocean is becoming more acidic; sea level is rising and this causes low-lying areas' floods.

The climate and weathering have changed drastically over the past few decades. Human activities are the main factor that causes climate change. Intergovernmental Panel on Climate Change (IPCC) presents detail information of global greenhouse gas emissions by gas as well as by sources as shown in figure 1 [2]. From the pie chart

shown in figure 1, we notice that the main sources of global gas emissions are carbon dioxide (CO_2), methane (CH_4), nitrous oxide (N_2O) and fluorinated gases (F-gases). Indeed, up to 77% of greenhouse gas is carbon dioxide generated either from fossil fuel usage or deforestation or so forth. In addition, 14% of methane and 8% of nitrous oxide are mainly due to agricultural activities either generated from fertilizer or waste. There are also up to 1% of gases are ejected due to industrial refrigeration of air-conditioner or refrigerator in which the device is consisted of hydrofluorocarbons (HFCs), perfluorocarbons (PFCs), and sulphur hexafluoride (SF_6) [1].

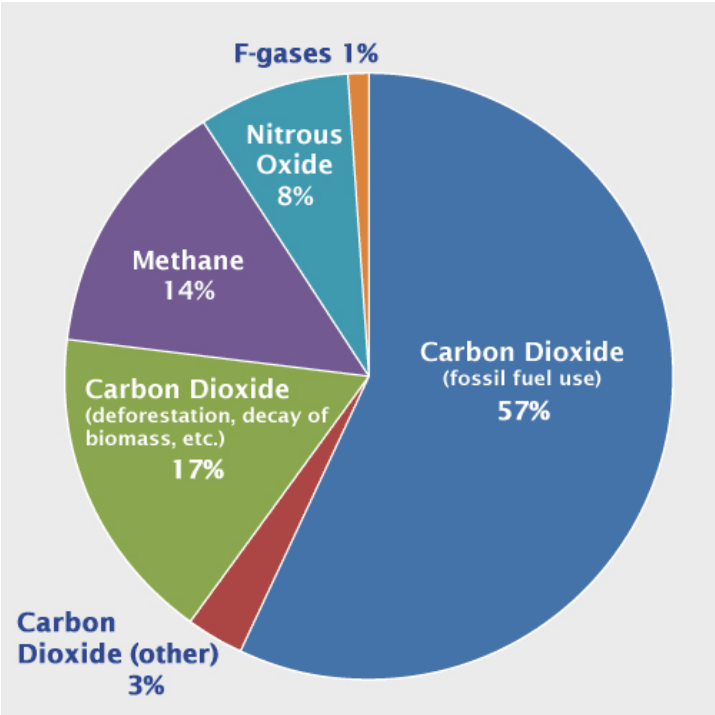

Figure 1.) Global greenhouse gas emissions from 2004 by gas

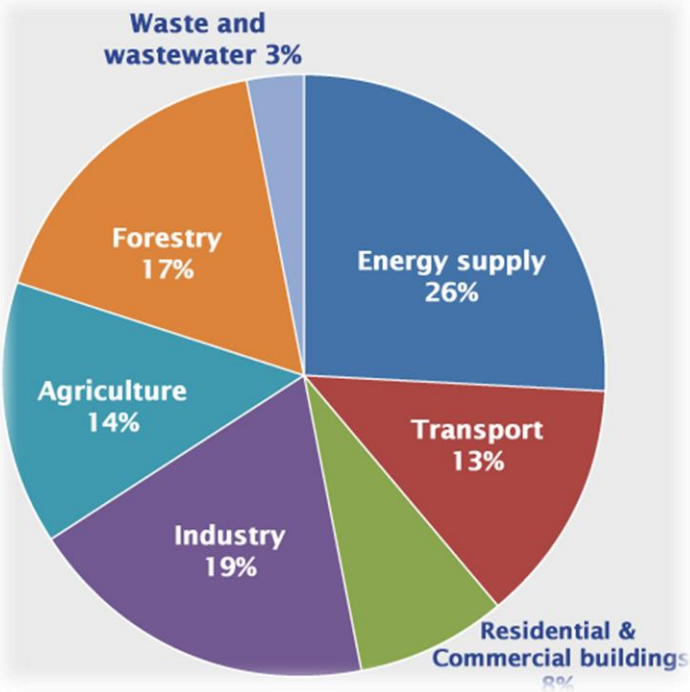

Figure 2.) Global greenhouse gas emissions from 2004 by source

IPCC also reported the global greenhouse gas emissions by source in 2007 as shown in figure 2. Refer to the pie chart as shown in Fig. 2, although only 26% of greenhouse gases sources are from energy supply, it is already one fourth of the total gases generation. In a deeper analysis, ejection of unwanted gases from transport and industry may also due to combustion of fossil fuel which emits up to 39% of the total emissions. Up to 31% of gases emissions are due to deforestation and agricultural purpose. There are also up to 11% of global gases arisen from the waste, wastewater and other residential and commercial buildings which may possibly due to usage of electricity. To sum up all factors, the portion can make up to about 70% which also implies most greenhouse gas is generated from various forms of energy usage that is related to the consumption of fossil fuels.

Global greenhouse gases emissions with the data shown in figure 3 were studied by Boden et al. [3]. Boden et al. presented the increment of the carbon dioxide over the past century. It is trivial to find that the emission of carbon dioxide has been increased by about 14 times for the past century. Refer to the graph as shown in Fig. 3, the trend of emission is rising drastically.

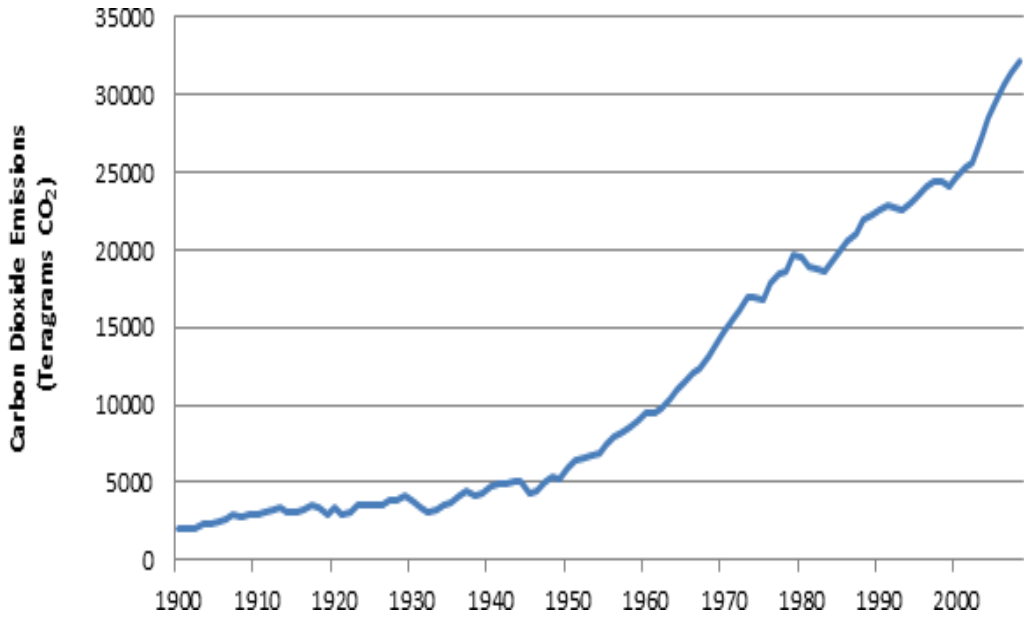

Figure 3.) Carbon Dioxide Emissions from 1900 to 2000

With the rapid increment of the emission of carbon dioxide, global warming has been becoming more crucial for people nowadays. In order to save our earth from severe atmospheric changes, promotion of reducing usage of electricity is not sufficient. Development of renewable energy supply must be implementing shortly to reduce the emission of greenhouse gases due to energy production. Renewable energy sources include biofuel, biomass, geothermal, hydroelectricity, solar energy, tidal energy, wave energy and wind power. Among developing various renewable energy sources, the development of the solar energy has been one of the most controversial technologies and is of the most concerned.

Nowadays, the price for renewable energy is still high as compared to conventional energy source such as fossil fuel. One of the biggest challenges in this century is to develop cost-effective and highly efficient renewable energy source to meet the global energy needs. IPCC has established that greenhouse gas emissions from fossil fuel

usage are most likely the primary cause for the excessive warming. Studies further show that a rise in temperature will have dramatic effects on our ecosystems. Furthermore, many scientists have been pointed out that continued dependence on fossil fuel will result in irreversible damages to the environment with devastating consequences. Fortunately abundant renewable energy sources are available on earth. Among all, the sun delivers over 86,000 TW of power to the earth. However, this renewable energy is still quite prohibitive to most people. Before the widespread of this renewable energy can come true, several breakthroughs, such as conversion efficiency and system cost, will be needed to be addressed. Thus fabrication of photovoltaic cells with good conversion efficiencies and low cost will be a grand challenge to both scientists and engineers.

1.2 Cost Trend of Solar Cells

Cost of electricity generated from different sources is always measured by $/Watt or euro/kWh through setup with the connection with loadings. The cost of the energy source highly depends on operation, fuel and maintenance of the devices.

The price of typical crystalline silicon photovoltaic cell has decreased from $76.67/Watt in1977 to about $0.74/Watt at present [4]. However the cost of photovoltaic energy source is still higher than that of conventional fossil fuel-based generated energy source. Moore's Law states that solar cell prices have significant decreased for every doubling of industry capacity which is similar to the Swanson's law stating that the cost of solar cells tends to drop 20% for every doubling of industry capacity [4] [5]. The Swanson's Law is named after Richard Swanson.

Different countries such as USA and Japan try to achieve grid parity in region with abundant sun light and expensive electricity [6]. George W. Bush, the previous president of the USA also set 2015 as usage of grid parity in the USA [7]. For the past 40 years, cost of the solar panels falls continuously in a stable rate. The demand for purified silicon was rapidly increased due to high subsidies from Germany for the computer chips and solar panel since 2004. With the attribution to the recession and the growth of Chinese photovoltaic industry, the cost of the solar panel had fallen. At present, the prices of the solar modules in Germany had fallen from 3 euro to less than 1 euro per peak watt. The production capacity surged with the increment for more than 50%. Besides, the market share of the China had increased from 8% to more than 55% in 2010 [8].

Even with the decrease in price of silicon solar panel, the cost of photovoltaic

energy is still high. Thus, high-efficiency photovoltaic cells are of great interest to lower the cost. One of the major costs of solar power plant ate correlated to the area or the amount of land used. In order to minimize plant area, high efficiency cells are desired so as to not only reduce the price of the solar panel but also the area occupied by for the solar panels. To obtain high efficiency, fundamental parameters such as short circuit current and open circuit voltage are important [9].

1.3 Introduction to typical Photovoltaic (PV)

Traditional solar cell consists of a p-n junction which was invented in late 1950s [10] [11] [12] and commercialized in 1960s for the involvement of space plan [13]. After that, drastically advanced was made in both the solar cell efficiency and reliability. This advancement not only drastically decreased the price of the solar cell but also expanded the solar cell industry in great extent. However the price of the solar power is still far higher than that produced by conventional power plants in different countries. Some argue that if the price included the price of the pollution caused by conventional power source, the cost will increase largely. Nevertheless, the researches on relatively cheaper types of solar cell like dyes and pigments are of increasing amount [14] [15] [16] [17].

Photovoltaic (PV) solar cells provide clean energy by directly converting sunlight into electrical energy without emission of carbon dioxide. Direct conversion of electricity from light energy highly relied on the photovoltaic effect. The term, photovoltaic has been used for more than 200 years [18]. It is a Greek word which can be subdivided into two parts known as “photo” (refers to light) and “volt” (refers to the unit of electromotive force). Electrical device such as solar cell or photovoltaic cell can be used to convert light to electric energy. Solar cell generates an electric current without any connection with external voltage source when it is exposed to intensive light source. There are many kinds of solar cells such as molecular semiconductor solar cells [19] and conducting polymer solar cell [20] [21] [22].

1.4 Mechanism and Exiton dissociation

The mechanism of typical solar cell relies highly on the formation of the p-n junctions. With semiconducting p-type materials and n-type materials stacking together, a p-n junction will be formed feasibly i.e. a p-n junction always appears in the interface between p-type materials and n-type materials. With the incident of light, high electrons concentration region is n-type region and high holes concentration region is the p-type region [12] [23]. After joining n-type material and p-type material together, the excess electrons in the n-type material will diffuse to the p-type material, and the excess holes in the p-types material will diffuse back to the n-type material. With this movement, an electron field is generated at the junction and the depletion region or space charge region will be formed as shown in figure 4 [24].

A voltage is also resulted from the charge separation appeared at the junction. Besides, there is a growth of majority carriers in the reverse direction and finally reaches an equilibrium.

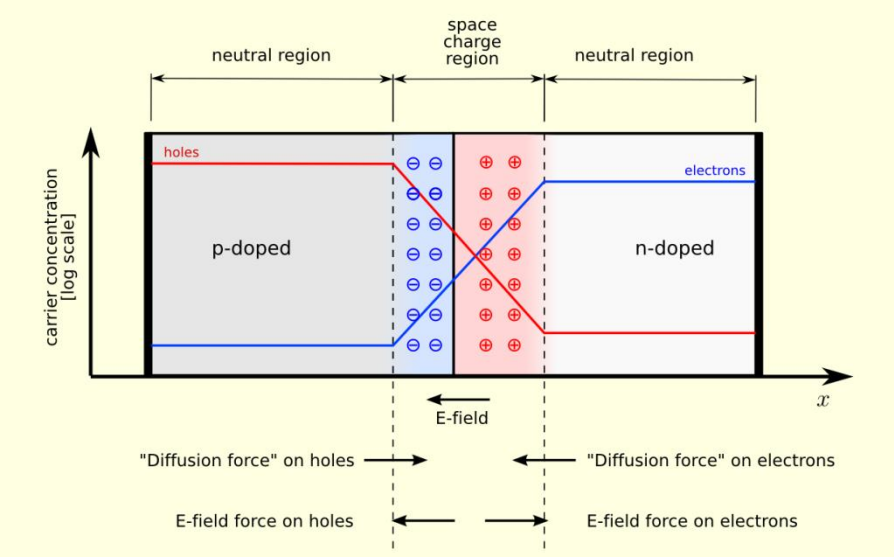

Figure 4.) Diffusion of holes and electrons and the build-up E-field

1.5 How photovoltaic effect works for solar cell?

Light energy travels in form of photons. The working mechanism of a photovoltaic cell or solar cell can be visualized by the schematic diagram as shown in figure 5 [24]. Photoelectric current mainly based on two processes: 1.) Creation of electron-hole pairs through absorption of incident photons, and 2.) Prevention of the recombination of generated carriers through spatially separating the holes and electrons. Photoelectric currents are generated inside the space charge area of the p-n junction. When the solar cell is exposed to light, the electron in the n-type region absorbed energy from light source. Then the electron is dislodged from the n-type semiconducting material and the free electron and holes are produced feasibly. When the light energy is sufficient, the free electrons and holes can break out of the depletion layer.

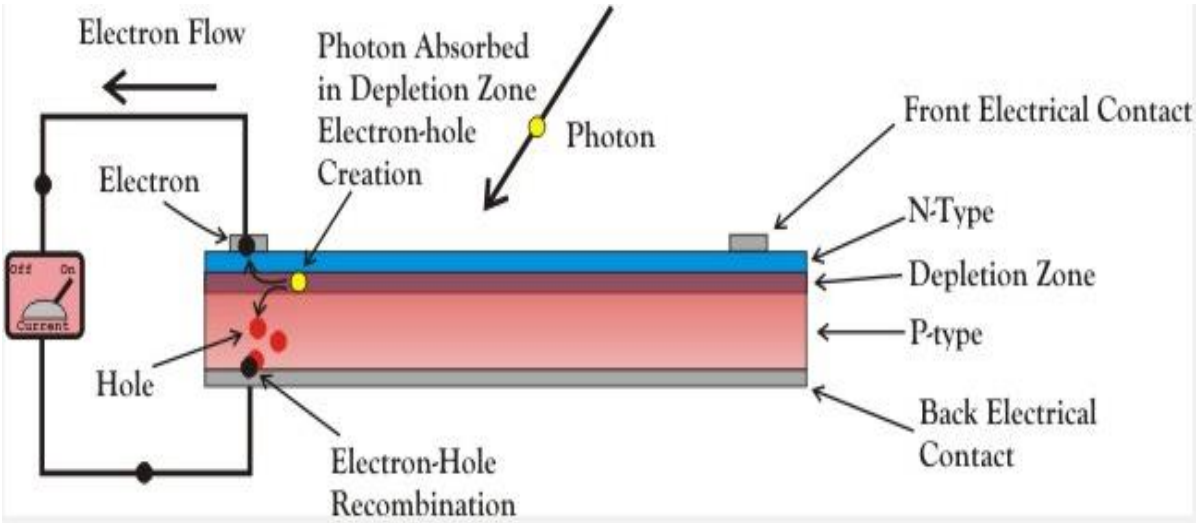

Figure 5.) Graphical working mechanism of photovoltaic cell

With the completion of the circuit between p-type semiconducting material and n-type semiconducting material, the flows of electrons will be from the n-type material to the p-type material corresponding to cathode and anode respectively. However, if the minority carriers flow across the p-n junction, the minority group will become majority carrier. With the connection of the base and emitter, the light generated carrier can flow through the external circuit instantaneously. The external electric circuit is to be completed through connection of electrodes on opposite sides with loading. Thus it results in electrical power.

1.6 History of Advancement of photovoltaic cell

Crystalline silicon solar cells have been extensively studied and used for various practical applications. To date, the highest conversion efficiency for single crystalline Si solar cell is around 27% and newly developed GaAs-based multiple junction solar cell has been reported with an even larger efficiency of about 40%. However, the expensive cost of these solar cells due to the complex fabrication process and the large consumption of energy during manufacturing have caused problems in term of high cost and long energy payback time. These problems prevent the wide spread of these solar cells for power generation. Therefore, a number of new material systems as well as device structures will be needed in order to accomplish the targets for renewable energy generation.

Recently, nanostructure solar cells, divided into inorganic and organic types, have been drawn a lot of attention. They are the third generation solar cells, desire to reduce the cost as well as increase the conversion efficiency based on NANOTECHNOLOGY. Nanowire-based solar cells have been reported to possess inherent advantages over traditional bilayer devices [25] [26] [27]. These nanostructure devices have large surface-to-volume ratio. By separating the optimal length scales for light absorption and exciton diffusion, it is possible to create a device with a relatively thick absorbing layer (for full solar spectral absorption), yet small interwire spacing (for short exciton diffusion) [28] [29]. Oriented nanowire arrays have been shown to possess excellent charge transport (and therefore charge collection) characteristics in PV devices [29].

Silicon, Cadmium sulfide (CdS), copper indium gallium selenide (CIGS) and copper zinc tin sulfide (CZTS) are the examples of inorganic materials that have been used in

the fabrication of thin film photovoltaics. At present, the advancement of the silicon solar cell is greatly hinder by the high expense, difficulties in high quality silicon films production on non-silicon substrates and also able to endure long time heat treatment due to its high temperature resistance. Different from the homojunction system produced by silicon, CIGS and CZTS are of high complexity heterojunction system. For CIGS, although the energy conversion efficiencies can be obtained up to 20%, the development of this compound is hindered by the lack of abundance of the precursor element, hard to produced semiconducting materials with high purity, also high cost and technology based and so on.

There are also many different kinds of photovoltaic cells have been reported by different laboratories as shown in figure 6 [30] [31]. Among all the solar cells, traditional silicon cell, multi-junction and thin film technologies using conducting materials such as CZTS and CdTe are the newest trends.

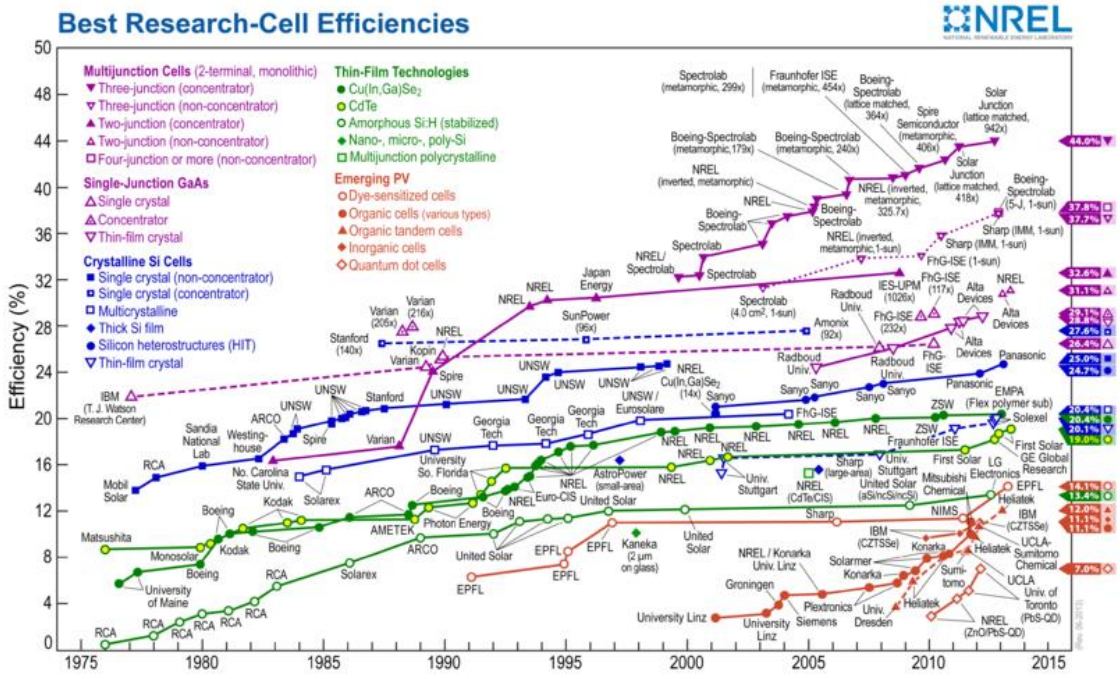

Figure 6.) Advancement of photovoltaic cells

Doped ZnO is a transparent conducting oxide and thus can be used either as a front or back side component in solar cells, depending on the substrate used and the geometry of contacts. The most widely used designs of ZnO based PV cells include addition of a light harvesting material such as organic dyes or inorganic absorbers with extremely thin thickness used for sensitization [32] [33] [34] [35] [36]. Material selection for future PV devices should satisfy several important criteria: They 1) should comprise of abundant and inexpensive elements; 2) should environmentally benign to avoid any issues of potential environmental contamination; 3) have an optimal band gap to maximize solar absorption such that the resulting solar cell would have a marketable energy conversion efficiency; and 4) can be synthesized easily. Among various light harvesting materials, one of the most promising candidates is the I-III-VI family. Among the I-III-VI family, $CuIn_{1-x}Ga_xSe_2$ (CIGS) is the most famous materials that are currently being commercialized for thin-film PV devices [37] [38] [39]. However, due to the limited supply and increasing price of rare metals, such as indium and gallium, there is a need to find alternative materials with high abundance and low cost. Recently, there has been an effort to investigate direct band gap Cu_2ZnSnS_4 (CZTS) and $Cu_2ZnSnSe_4$ (CZTSe) thin films for PV applications due to their particular advantages: They 1) contain earth-abundant elements (cheap and non-toxic); 2) have a near-optimum direct band gap energy of around 1.5 eV; 3) own a large absorption coefficient (>104 cm^{-1}) and 4) possess a large theoretical limit of energy conversion efficiency (32% for CZTS) based on Shockley-Queisser photon balance calculations [40] [41] [42]. Studies have been reported on the fabrication and PV properties of CZTS nanocrystals using high-temperature arrested precipitation in coordinating solvent

method [43] [44] [45]. However, up to now, there are no reports of synthesis of CZTS nanocrystals using low temperature (energy saving) fabrication method which is important in reducing the energy payback time.

1.7 History of semiconducting materials through electrodeposition

Single elements electrodeposition has been developed for centuries in extracting different kinds of metals ores such as gold and silver. This technique is also widely used in fabrication or maintenance of luxury products to produce shinny surface. Electrodeposition of semiconducting materials was first introduced in 1970s [46] [47]. Early in the 1980s, researchers have been developing a thin film solar cell with the usage of electrodeposition with reasonable efficiency. With the stimulation of this work, research interests in electrodeposition were on heat, especially the electrodeposition of the semiconducting materials. At that time, Basol [48] presented a great work of thin film electrodeposited CdS/CdTe on CdTe substrate. This solar cell had efficiency up to 10%. For the past two decades, researches switched their focus on III-V, I-III-VI_2 materials and other alloy semiconductors as well, especially on II-VI semiconductor. Since then, the development of electrodeposition has extended to other material of certain hardness such as silicon and even nitrides. The advancement of the electrodeposition is beneficial for fabrication of thin film solar cell and it also builds up a platform for researches to further discover. Most current established film growing technique involves a two steps process. The ceramic material is first synthesized in bulk structure. The ceramic material is then pressed into a target and will be irradiated by a high-power laser, an ion electron beam or even a rf source. The resulting sample will then be captured onto a cold substrate. These techniques require high power source or ultrahigh vacuum systems in order to produce extremely intensive energy source. However, these techniques are inapplicable when the substrate material is of low temperature phase due to occurrence of instantaneous deposition of the substrate

material. There are many types of thin film electronics methods. Molecular beam epitaxy (MBE) systems or metal-organic chemical vapor deposition (MOCVD) systems that are well established needs to have a cost up to £1 million. There are also ceramic thin film techniques with involvement of current including pulse laser deposition, radioactive frequency sputtering, and electron beam etching [49] [50] [51] [52] [53]. These systems limit the number of different materials to be grown. Comparing the cost of a computerized potentiostat to other thin film deposition techniques, a computerized potentiostat costs a few ten times less and even as low as £5000.

The similarity of the electrodeposition of semiconducting materials is similar to the electrodeposition of metal which also subjected to an electrolyte containing appropriate ions and three individual electrodes. To be more specifically, the extrinsic doping can be easily achieved through the addition of accurate amount of dopants into the electrolyte. Meanwhile, the intrinsic doping materials can also be obtained simply through modifying the composition of the electrolyte. It is also possible to adjust or tune the band gap of the semiconductors which can be visualized based on the optical absorption spectrum. The PH value, temperature and applied voltage of the electrolyte can also change the morphology of the desired materials.

Physical deposition methods involve gas-to-solid phase conversion growth process. However, liquid-to-solid phase transition is more feasible to process in nature [54]. Since the potential gradient of cathode surface can attain up to 10^5 Vcm^{-1} within the electric double layer to give excellent growth condition, the thin film material produced is of good quality. Once the neutrality during the growth has been satisfied, many other shapes hardly obtained from other techniques can be easily produced.

Electrodeposition is also a low temperature processing technique in which the base electrolyte is usually water based, thus the operating temperature is normally under the boiling point of water.

The principle of electrochemical synthesis in brief is usually based on redox reaction of different species in the electrolytes and can be classified into thermodynamic control and kinetic control. Through modifying the applied cell potential, steps with either constant oxidizing or reducing power will be chosen. The exercised of thermodynamic control known as the potentiostatic synthesis which tends to yield single phase pure product. Unfortunately, the current always decays rapidly once the reaction rate hit its low and it also attributes to the low diffusion rate of the reactant and decreases in reactant activity. Whereas the kinetic control can be achieved by varying the current passes through the cell to give galvanostatic synthesis leading to the production of film with excellent adhesion and variety of morphology.

Typical types of electrosynthetic techniques and the natural products to be obtained from different techniques are listed in Table 1. [55]

Table 1.) Summary of the Electrosynthetic Techniques Employed in Inorganic Solid-State

Technique	Product	Application
1. Electromigration of reactant species	Polycrystalline powders/ single crystals	Battery electrode materials
2. Electrolysis of fused salts	Single crystals	Crystal growth at moderate temperature
3. Electrogeneration of base by cathodic reduction	Coatings/ films/ powders	Synthesis of electrode materials for secondary cells, fabrication of hydroxide films/ coatings
4. Anodic oxidation	Coatings/ films/ powders	Synthesis of compounds with high oxidation state
5. Alternate current synthesis	Layer-by-layer films/ coatings	Synthesis of composites/ solid solutions

1.8 Objectives

In this proposal, we present a novel solar cell design that combines the ideal geometry of ZnO-based nanowire solar cells with the concept of using environmentally friendly, inexpensive, and durable semiconducting PV components (CZTS and CZTSe). Our solar cell consists of vertically oriented n-type ZnO based nanowires, covered by a film constructed from p-type inorganic materials (CZTS and CZTSe) nanoparticles (NP) as shown in Fig. 7.

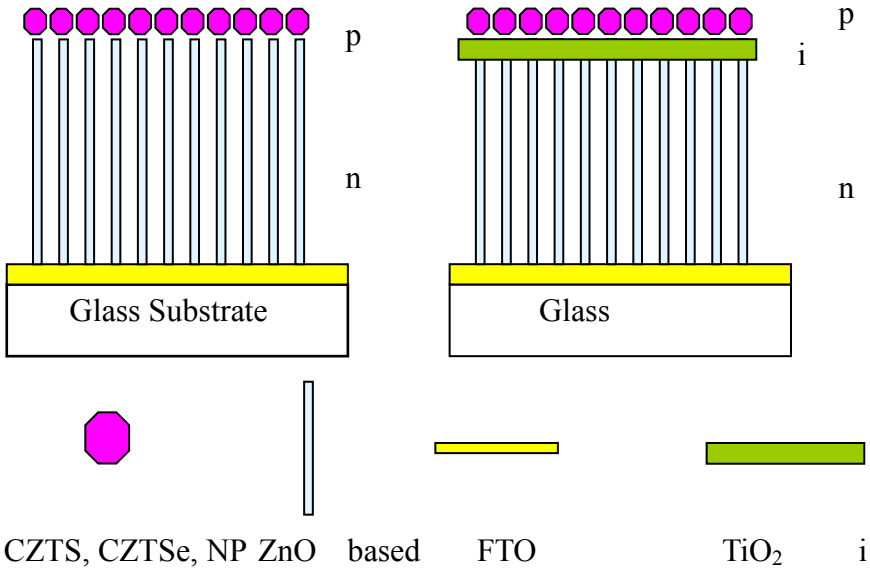

Figure 7.) Solar cells: ZnO-based nanostructured all-inorganic solar cells

The above design is based on a two-dimensional (2D) planar substrate. As mentioned before, this nanowire-based solar cell has large surface-to-volume ratio, and should out-perform the traditional bilayer structure. Furthermore, in order to enhance the surface area for the interaction of light and then the energy conversion efficiency, we attempt to extend the 2D solar cell geometry to 3D cell geometry by growing ZnO based nanostructured solar cells on optical fibers. Figure 8 shows the design and

principle of a 3D solar cell integrated on fibers. The light illuminates the fiber from one end along the axial direction, and its internal reflection within the fiber creates multiple opportunities for energy conversion at the interfaces [20]. Moreover, these 3D solar cells can be remotely controlled through fiber. By depositing different solar optical absorption materials, which have different optical spectrum absorption ranges, on ZnO based NWs at different sites, we can further fabricate a 3D solar cell whose absorption range can cover all the solar spectrum range. Undoubtedly, this proposed 3D solar cell will possess improved energy conversion efficiency.

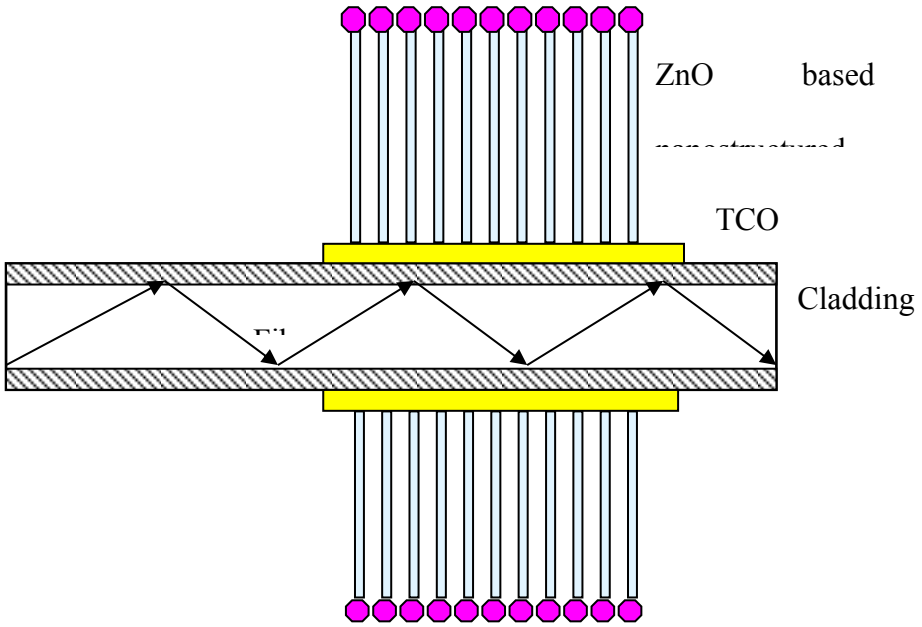

Figure 8.) ZnO based nanostructured solar cells on fiber

Chapter 2 Literature Review

2.1 Zinc Oxide (ZnO)

The development of zinc oxide (ZnO) has been advanced for the past hundredth of years and can be traced back to 1935 [56]. From a surge of publications, it is not uncommon to see many interests generated from semiconducting ZnO. ZnO is of importance as a multifunctional semiconductor emerged with a very wide direct band gap of 3.3 eV. With its band gap energy overlapping with GaN which is also a wide band gap semiconductor of about 3.4 eV at 300K, ZnO has been widely used for making green, blue-ultraviolet and white colored light-emiting devices (LED). ZnO also has a very big exciton binding energy up to 60 meV under room temperature condition. ZnO belongs to the II-VI compound semiconductor whose iconicity is in between covalent bonding and the ionic bonding semiconducting material. Just like other II-VI semiconducting materials, wurtzite ZnO can easily convert to rocksalt (NaCl) structure under moderate pressure. This may possibly due to the reduction of the lattice dimensions causing the interionic Coulomb interaction to favor the ionic characteristic and is more over the covalent nature. The disadvantage is that the rocksalt structure cannot be stabilized by epitaxial growth. The normal structure of ZnO can be divided into three types, wurtzite (B4), zinc blende (B3) and rocksalt (B1) which can be visualized as the following figure.

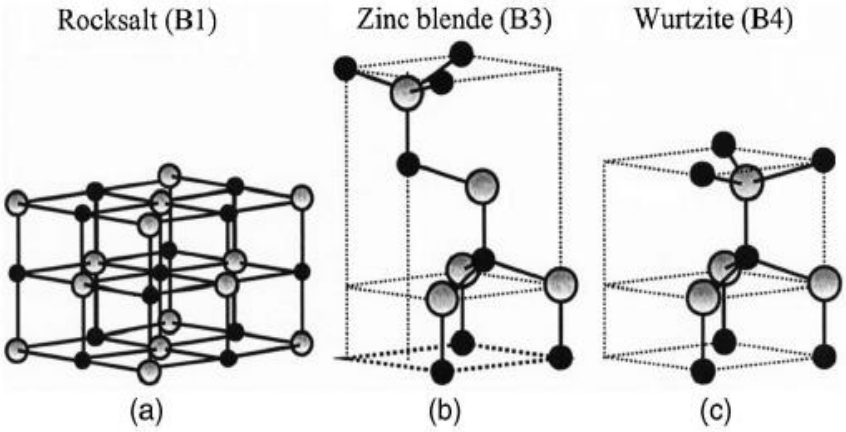

Figure 9.) The ball and stick representation of ZnO crystal structures: (a) cubic rocksalt (B1), (b) cubic zinc blende (B3), and hexagonal wurtzite (B4). And the shaded gray and black spheres denote Zn and O atoms respectively.

Wurtzite structure is thermodynamically stable under ambient condition. Zinc blende can be obtained when the coated substrates are of cubic phase. Rocksalt structure is more favorable with the increase in environment pressure [57]. For ZnO, the most common structure is of wurtzite type which has hexagonal unit cell with the two lattice parameters a = 0.325 nm and c = 0.521 nm, i.e. the ratio of c to a is 1.633. This means that it belongs to the space group of C_{6v}^4 or $P6_3mc$ [58] [59] [60] [61]. In the wurtzite structure, four cations are at the coners position rounds the anion and the bonding between the cation and anion is typically of covalent bonding with substantial ionic nature. The schematic representation of a wurtzitic ZnO structure having lattice constants a in the basal plane and c in the basal direction are shown in figure 10 [57].

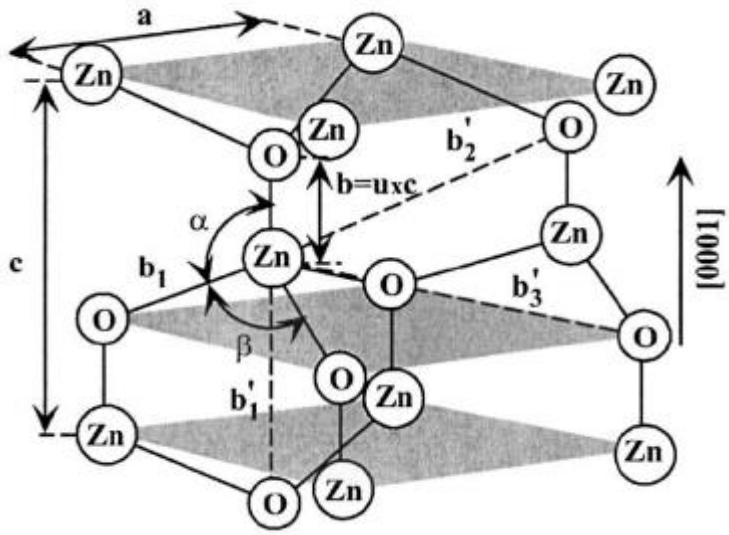

Figure 10.) Schematic representation of a wurtzitic ZnO structure having lattice constants a in the basal plane and c in the basal direction; u parameter is expressed as the bond length or the nearest length or the nearest-neighbor distance b divided by c (0.375 in ideal crystal), and α and β (109.47^o in ideal crystal) are the bond angles.

The lattice parameter of a semiconducting material typically depends on the following four factors [57]: (i) free-electron concentration acting via deformation potential of a conduction-band minimum occupied by these electrons, (ii) concentration of foreign atoms and defects and their difference of ionic radii with respect to the substituted matrix ion, (iii) external strains especially induced by substrates, and (iv) reaction temperature. Zinc oxides itself have different distinct properties that raises many research interest. Lattice constants of ZnO under room temperature condition also have been widely determined either in experimental or theoretical and is of good

agreement. Most found lattice constants are of range from 3.2475 Å to 3.2501 Å for the *a* parameter, and 5.2042Å to 5.2075Å for *c* parameter [62]. The variation of ideal wurtzite crystal may possibly due to lattice stability and its ionicity.

Zinc oxide contains high ultra-violet absorbance, wide chemistry, large piezoelectric properties and a strong luminescence effect under high temperature. Regarding to its uniqueness such as optical, acoustic, luminescent, and electronic and optoelectronic properties, ZnO is of popular in the application of industrial area. At present, many methods have been presented for the preparation of ZnO material as an one-dimension (1D) nanostructures with different kinds of morphologies such as nanowires, nanorods, nanotubes, whiskers, nanocrystals, nanobelts, nanoflowers and other specific nanostructures [58] [60] [63]. It is also not uncommon to find ZnO in paints, cosmetics, plastic and rubber manufacturing, electronics and pharmaceuticals and other daily products. ZnO itself is also a transparent conductive oxide (TCO) that is an indispensable material for electrodes in optoelectronic devices such as lasers, acoustic and optical devices with very short wavelength. There are also application of piezoelectric transducers, actuators and photovoltaic cells [60] [61] [63] [64] [65] [66].

ZnO as mentioned before is not a new material and its structural properties, refractive index and optical as well as other properties have been investigating for many decades [56] [67] [68] [69] [70] [71] [72] [62]. Several methods to synthesis ZnO nanostructure have been reported, such as vapor transport process catalyst free or catalyst assisted epitaxial electrodeposition, solution gel method, metal-organic chemical vapor deposition (MOCVD), pulsed laser deposition (PLD), aqueous chemical methods or simply hydrothermal methods [58] [65] [66]. The low temperature

hydrothermal synthesis and the electrochemical deposition are of convenience and economic for well aligned ZnO nanorods and nanowires. However, due to environmental issue, the temperatures used the hydrothermal process and electrochemical deposition process should remain as low as possible. The typical hydrothermal process temperature used for the fabrication of ZnO is from 150^{o}C to 250^{o}C. The electrochemical process for the fabrication of ZnO is about 80^{o}C. In recent years, ZnO has also been widely used as the transparent thin-film transistors which coated with the ZnO to prevent the exposure to the visible light since ZnO is not sensitive to the visible light. Furthermore, through doping with different dopants, the charge carriers concentration of ZnO up to 2×10^{21} cm^{-3} can be easily produced. With the doping in different extents, depends on the doping level, the electrical properties can be changed from insulator through n-type semiconductor to metal while maintaining its optical transparent. It is useful to be used as transparent electrodes in flat-panel display and solar cells.

2.2 Copper Zinc Tin Sulfide (CZTS)

Nowadays, the first generation of solar cell (Si) has been commercialized for many years and is dominating the photovoltaic (PV) market. However, high quality Si substrates with thickness over 150 μm consists high-cost purifying process. This definitely increases the price for the solar-to-electric energy conversion. The reasons for having a thick Si substrate are due to its indirect band gap with very low absorption coefficient, so sufficient thickness is required to trap the light. With the advancement of the semiconductor film in the past few decades, the thickness of the crystalline indirect band gap Si can be narrowed down to about 1-3 μm comparing to the conventional one. The recent thin film Si device is thinner for more than thousand times, leading to a decrease of cost. Besides using Si, other materials are also employed in developing thin film solar cells. The technology of thin film solar cell is estimated to lead the photovoltaic market in latest 2015 with the use of cadmium telluride or copper indium gallium diselenide (CIGS) as the absorbing material. However, some researchers argue that the production of the thin film solar can only be limited to 1 TW due to the scarcity of Te and In as well as Cd [73] [74] [75]. Furthermore, these elements are also toxic and hazard to the environment. The lacks of the existing thin film solar cells absorbing material have raised many concerns, meanwhile, evokes many strong motivation for developing new materials with nontoxic and abundant elements.

Among various I-III-IV materials, copper zinc tin sulfide (Cu_2ZnSnS_4/CZTS) is one of the hottest potential light absorber in the next generation thin film solar cells due to its nontoxicity and high abundant elements [75]. Cu_2ZnSnS_4 presents similar properties and electronic effects as those of CIGS in which CIGS possesses high energy conversion of

20% [76] [77] [78]. CZTS has a tetragonal structure known as the kesterites. According to Chen et al., CZTS belongs to the space group *I4* with the lattice parameters of a = 0.5467 nm and c = 1.0923 nm [79]. CZTS thin films were synthesized by sulfurizing a stack of zinc, copper and tin films. IBM has been performing researches on CZTS in the last decade and demonstrated the potential of CZTS as solar cell [80]. Typically, CZTS were reported to have direct band gap energy between 1.45 eV to 1.6 eV. This wide variation in the band gap energy can attribute to variations in the stoichiometry of the material [81] [82]. In order to take advantage of the dense solar spectrum, CZTS is always optimized with its band gap. It is trivial that CZTS had absorption coefficient up to $10^4 cm^{-1}$ making it ideal for thin film devices [82]. The tetragonal crystal structure as shown in fig. 11 was derived from the CIGS crystal with the substitution of two indium or gallium ions by one zinc and one tin atom. P-type semiconducting CZTS has charge carrier concentration of approximately 5×10^{16} cm^{-3}. Schockley-Queisser calculation has a maximum theoretical efficiency limit for about 32.2% and recent reports also showed that the measured efficiency of practical CZTS developed was up to 11.1% [83]. First CZTS thin film solar cell was reported with an efficiency of about 0.66% in 1997 by Katagiri et al [84]. Within a decade time, drastic increase in the improvement of CZTS solar cell had advanced its efficiency up to 6.77% [85]. After less than five years, Todorov et al also demonstrated that CZTS solar cell fabricated by novel slurry-based thin film deposition method with power conversion efficiency up to 9.66% was obtained [83]. The manufacturing marketable efficiency is 10% and the current efficient goal for CZTS is between 12 % to about 15%.

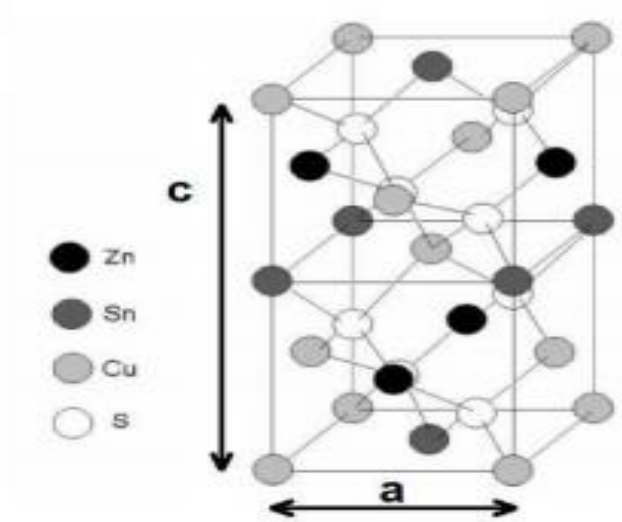

Figure 11.) Kesterite structure in which CZTS crystallizes. It is derived from the sphalerite structure by duplicating the unit cell [86].

2.3 Development of Electrodeposition

The process used in electroplating is also known as electrodeposition which is analogous to a galvanic cell acting in reverse direction. A schematic diagram of electrodeposition is shown in figure 12.

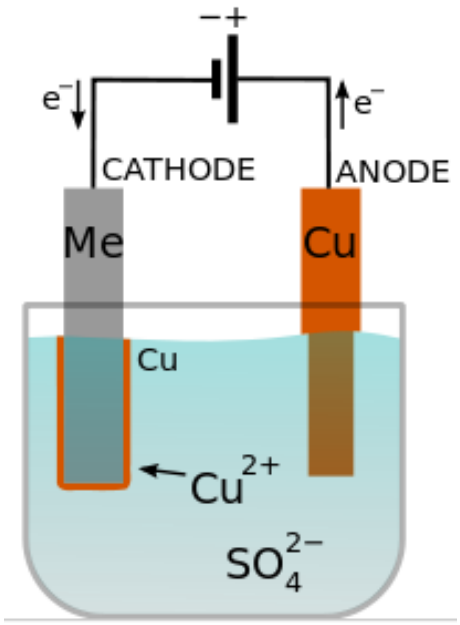

Figure 12.) Electrodeposition of copper in a copper sulfate bath

The sample to be plated will be subjected to cathode of the circuit whereas the metal plate to be plate on the sample will be subjected to the anode. Both anode and cathode are dipped into a solution named electrolyte to consist of at least one dissolved metal salts and other ions in order that the electricity is allowed to flow. Typical electrodeposition setup should consist of a bath with two electrodes in it. Electrodeposition is a process with the usage of the current to reduce dissolved metal cations so that they form a coherent metal coating on an electrode and also a counter

electrode. This can also be treated as electrical oxidation of anion onto a solid substrate. The cations and anions move from the cathode to anode and vise versa respectively. The main purpose for the usage of the electroplating is to change the surface properties of different materials and building up a certain thickness undersized. A source is connected to the anode and supplies direct current anode to oxidize metal ions. The metal ions in the electrolyte solution will be reduced at the interface between the solution and the cathode.

However, the mechanism of electroplating can be traced back to hundreds years before. In that day, Michael Faraday was famous for the law of electrolysis: Faraday's First Law and Faraday's Second Law. Faraday's First Law states that the total amount of chemical changed appears by an electric current is proportional to the total charge through the electrolyte. The masses of the different substances in the electrolysis are proportional to their chemical equivalent weights. The mathematical expression of first law is shown as follows:

Equation 1 $$\Delta \mathbf{m} = \boldsymbol{C_e j t}$$

Where C_e is the chemical equivalent constant, Δm is the mass deposited on a unit area, j is the current density flowing in the electrolyte, t is the deposition time. The mathematical expression of Faraday's Second Law is shown as follows:

Equation 2 $$\frac{\boldsymbol{d}}{\boldsymbol{dt}}\Delta \boldsymbol{m} = \boldsymbol{C_e j} = \frac{\boldsymbol{M}}{\boldsymbol{zF}}\boldsymbol{j}$$

Where F is the Faraday's constant, M is the molar mass of the electrodeposition and z is the ionic charge. Substitution of equation 2 to equation 1, Δm can also be written as follow as equation 3.

Equation 3 $$\Delta m = C_e jt = \frac{M}{zF} jt$$

The electrolyte can either be aqueous, nonaqueous or molten, but it must electrically conductive and provides suitable metal slats in the electrolyte for elctrodeposition. At least two electrodes anode and cathode are fundamental in electrodepostion process as the applied electric field across the electrodes is the main driving force for the ions. To be simple, positive ion and negative ion will be deposited at the cathode and anode respectively. Cathodic deposition is famous in electroplating since most metal ions are positive ions whereas anodic depositions were found to be poor adhesion [87].

2.4 X-Ray Deflection (XRD) mechanism

X-ray is an electromagnetic radiation and the typical photon energies are from 100 eV-100 keV. In diffraction application, only short wavelength x-rays will be used and the wavelength can possibly narrow down to even 0.1 Å and functional voltage applied here can be from 1 keV-120 keV. Since the wavelength used in the x-ray is comparable to the size of an atom, the arrangement or modulation of atoms and molecules of different kinds of materials can be determined. X-ray penetrates deep into the materials so as to probe the bulk structure of the materials.

X-ray is produced by synchrotron radiation which is also known primary x-ray used in laboratory x-ray instrument. Generation of the x-ray through the accelerate electron beam across the high voltage field causing bombardment on a stationary target. After the electron colliding with the atom and it will slow down to give continuous spectrum of X-ray and is known as the Bremsstrahlung radiation. Common targets in the x-ray tube are Cu and Mo in which they emitted 8 keV and 14 keV x-rays with corresponding to 1.54 Å and 0.8 Å respectively.

Photon of the x-ray interacts with the electrons and deflected away from the incident direction. If the scattering does not consist of the loss of energy and the wavelength of the scattered x-rays remain the same, it is known as elastic scattering or Thompson Scattering.

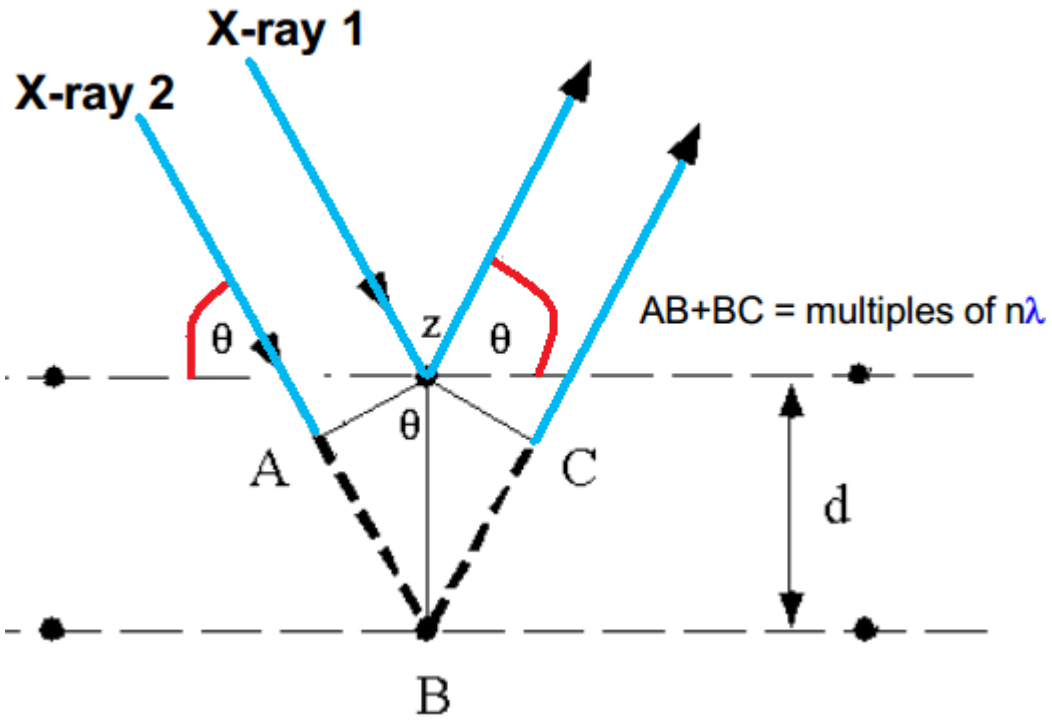

Figure 13.) The schematic diagram of the X-ray Diffraction inside the crystals.

As shown in figure 13, the X-ray, incident on a sample, interacts with the electrons inside the atoms to give scattering X-ray. With the constructive and destructive interference of the incident ray and scattered ray, the specific material structures can be reviewed. In general, if the incident ray and the scattered ray are out of phase, destructive interference occurs. If the incident ray and the scattered ray are in phase, constructive interference occurs. This feature always follows Bragg's Law [87]:

$$n\lambda = 2d \sin\theta$$

Here n is an integer, λ is the wavelength of the incident X-rays with wavelength of 0.154 nm, θ is the amount of angles deflected and d is the spacing between the atom planes. Analysis of the diffraction pattern is crucial. The deflection angles obtained

from the X-ray diffraction pattern are the 2θ. Different peaks can be correlated to different crystal planes separation. The width, intensity and the location of the peak also provides the information of the specific phase and crystal sized and variation. It is also well known that the broader the peak is, the smaller the crystal size.

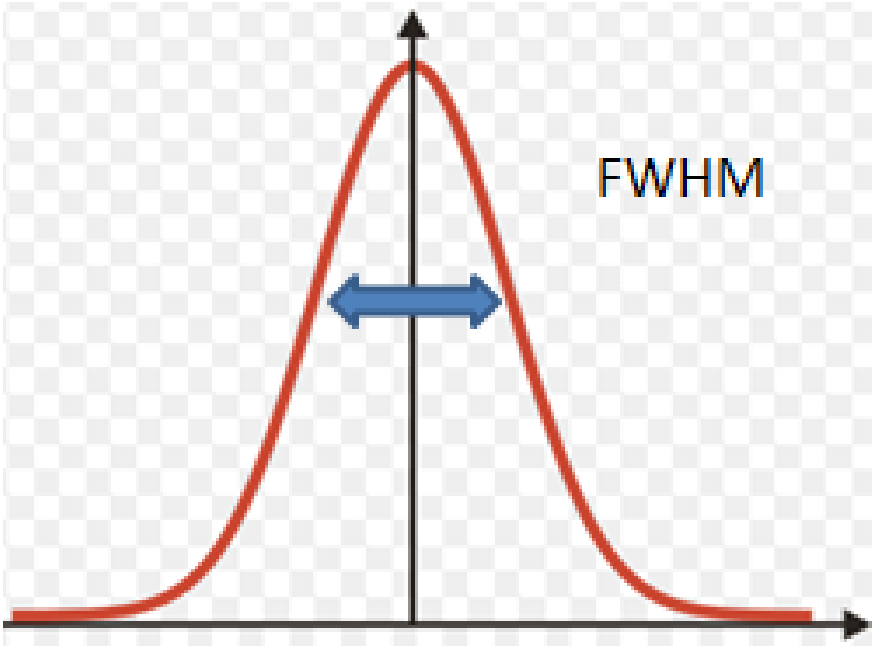

Figure 14.) Gaussian x-ray diffraction peak profile

Crystalline size of particular peaks can be calculated using the Scherrer equation [88] [89]:

$$L=\frac{0.9\lambda}{\beta cos\theta}$$

Where λ is the wavelength of the X-ray used (0.154 nm in our case), β is the full-wave half-maximum of the X-ray peaks, L refers to the average crystalline sized and k = 0.9 and is a constant. It is also noticed that only particles with grain size less than 100 nm can be accurately determined by Scherrer equation.

2.5 Scanning electron microscope (SEM)

Scanning electron microscope (SEM) is a high resolution microscope that produced images of samples with the incident of a beam of electrons. For the past half century, electron microscopy has become a powerful method of studying and analyzing microstructure of materials. SEM is a simple and useful technique for the study of the surface morphology. Hence, SEM has become a routine technique in most industrial laboratories in order to visualized the fracture surfaces, welds, surface finishing, powder sized distribution and even the lithographic pattern. SEM and XRD are supplement in the analysis of different composition of small particles. Typical SEM can be used in at least three different modes: voltage contrast, cathodoluminescence and the electron beam-induced current mode.

Generally, secondary electrons with energies less than 50 eV and the trajectories from the specimen surface to the detector are affected through varying the surface potential which is biased at +5V. In which the energies of electrons less than 5eV cannot reach the detectors and leads to no contribution to the final image. If part of the specimen is subjected to negative potential comparing to others, they will be bring in SEM image which also tells that the low energy secondary is boosted by negative bias. This phenomenon is also known as voltage contrast. Besides, cathodoluminescence is the electron-hole pair generated from high energy electrons and recombined to give light energy leading to SEM image of the specimen surface. Since the colors generated highly depend on the band gap structure, this can be strengthening strategy for the phase identification especially for rock or minerals. The electron beam-induced current mode is the primary beam creates electron-hole pairs in semiconductors. If the pairs formed

close to p-n junction, the local field leading to these carriers to be collected. Since the recombination usually located in the dislocation in preference to within perfect regions of crystal, the dislocations can be visualized through the electron beam-induced current mode.

How scanning electron microscope?

Shorter wavelength electrons are used in SEM compared with visible light used in optical microscopy in order to produced image of higher resolution. In an SEM chamber, the electron generated from the filament electron gun is accelerated towards the samples which act like anode. The samples must be conducting to prevent accumulation of charges. However, most samples to be investigated are of non-conductive. Thus a thin layer of gold is sputtered on the surface of the sample to pass the current. When high energy electron is bombarded with the sample surface, the electron of the outermost layer will be detached from the samples. The detached electrons or secondary electrons are of lower kinetic energy and are more readily to be attracted by the detector. The detectors counts the number of electrons emitted from the small area and records the corresponding origination location of each point. The resulting information of image is obtained and displayed on the computer screen. The image shown has shadow and perspective and is of image depth which is just like normal photograph. This also helps the interpretation of SEM image. The typical structure inside the SEM can be visualized in figure 15.

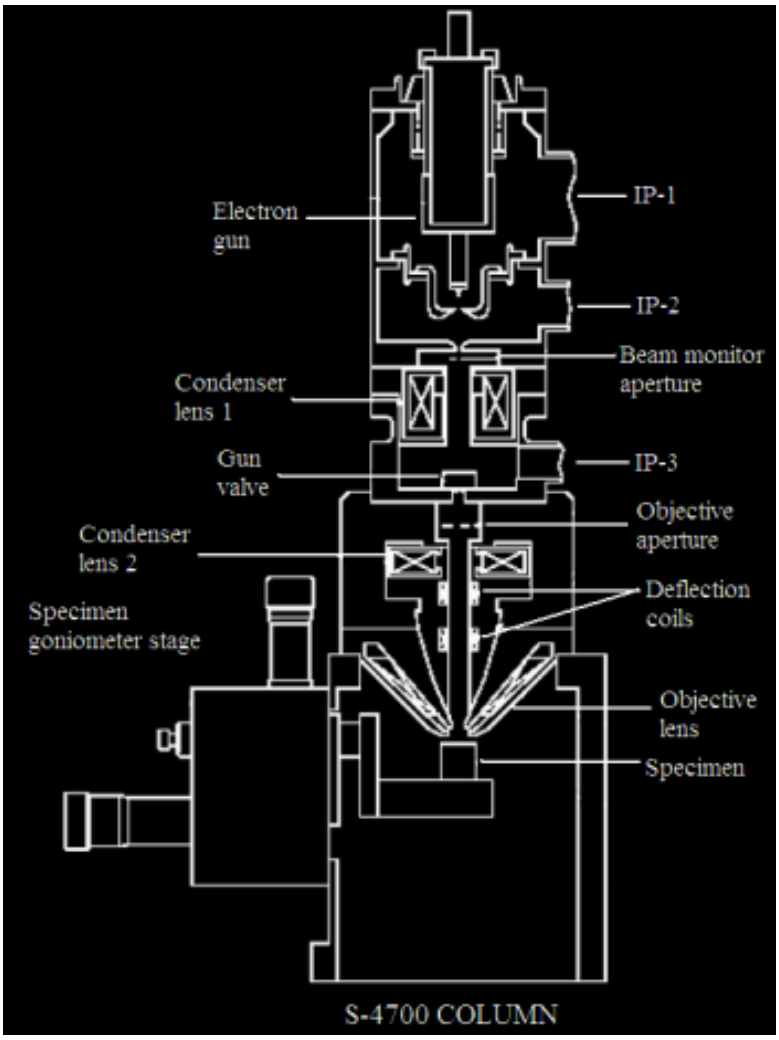

Figure 15.) The internal structure of typical SEM set-up

2.6 Transmission electron microscopy (TEM)

Transmission electron microscopy (TEM) is a microscopy technique in which a beam of higher energy electron is transmitted across and interacted with the ultra-thin specimen to give an image. There will be an image obtained and magnified on fluorescent screen which will be detected through a CCD camera. The mechanical structure of the TEM is similar to that of SEM. TEM consists of an emission source such as tungsten filament [90]. Through connecting the small spike shaped filament to the high voltage source (100keV-300keV) gun and sufficient current in vacuum, the electrons begins to emit either by thermionic or field electron emission. After the modification of a series of electromagnetic lens, the signal can be used to generated image of a few angstroms or converted into electron diffraction spectrum to determine the microscopic crystallographic structure. The sketch of image and diffraction mode within TEM arrangement can be visualized in figure 16.

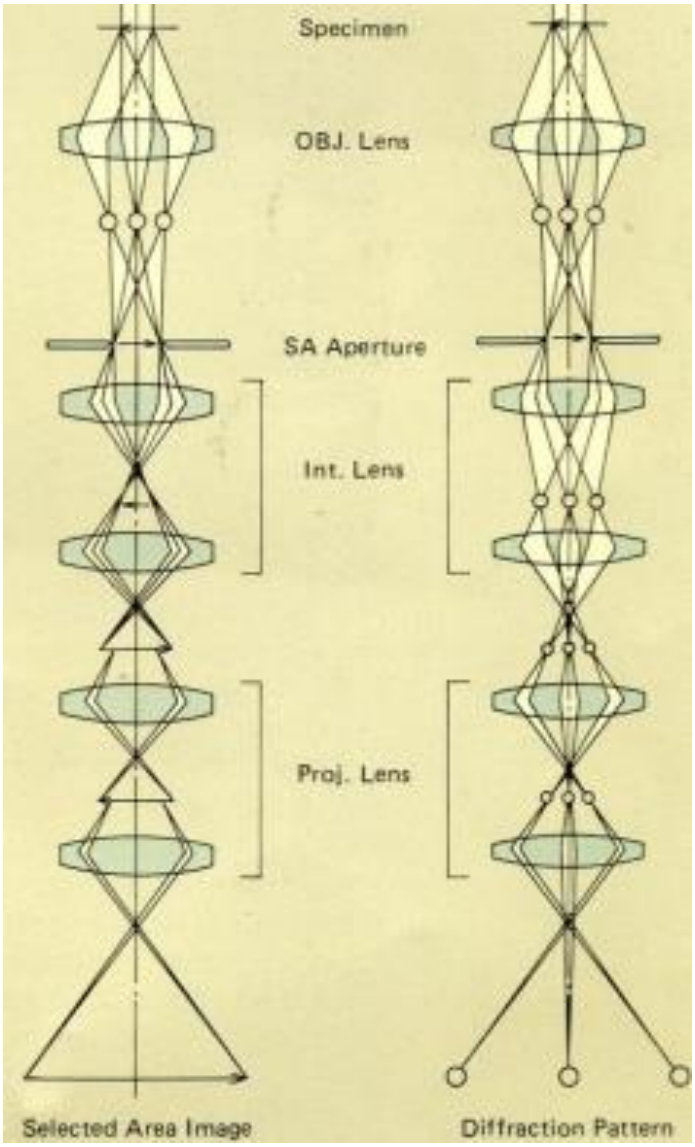

Figure 16.)Sketch of image and diffraction mode within TEM arrangement

Chapter 3 Fabrication of Zinc Oxide (ZnO)

3.1 Introduction to experimental set-up

In this project, ZnO was fabricated through electrodeposition method using potentiostat. The solution $Zn(NO_3)_2$ concentration was 0.01M and the target voltage of the potentiostat was varied between -0.5 V and 1.5 V. The temperature of the electrodeposition was at 80 ^oC. The reason for choosing this temperature was that if the temperature is too low, the reaction cannot start up; however, if the temperature is too high, the evaporation of water may have great effect on the stability of the solution. In this case, we chose 80 ^oC [92] .

The $Zn(NO_3)_2$ powders were first dissolved into 500 cm^3 of DI water to achieve a solution with concentration varying from 0.01M to 0.1M. Then the solution was heated on a hotplate together with a water bath for about half an hour so that the temperature maintained at about 80 ^oC. After that, the ITO/PET substrate was connected to the working electrode. The counter electrode was graphite and the reference electrode was AgCl. The resulting thin film formed was taken out from the $Zn(NO_3)_2$ solution and was rinsed with deionized water for several time. Finally, the samples were put into an oven at around 100 ^oC for 8 hrs to dry up the film. In order to produce ZnO of better crystallinity, lower temperature down to 60^oC [93] and longer heating time of more than 4 hrs were required.

The electrodeposition reaction follows the chemical reaction shows as follows:

$$\text{Step 1: } NO_3^- + H_2O + 2e^- \rightarrow NO_2^- + 2OH^-$$

$$\text{Step 2: } Zn^{2+} + 2OH^{-} \rightarrow Zn(OH)_2$$

$$\text{Step 3: } Zn(OH)_2 \rightarrow ZnO + H_2O$$

$$\text{Overall reaction: } NO_3^{-} + Zn^{2+} + 2e^{-} \rightarrow ZnO + NO_2^{-}$$

The above chmical reactions show a redox reaction. With sufficient electrons produced, the OH^- ion was generated from the reduction of nitrate ions. Then the Zn^{2+} ions combines with the OH^- ions to give zinc hydroxide which is a meta-stable state of zinc consisting compound. Finally, in order to reach the stable state, zinc hydroxide was feasibly decomposited into water and zinc oxide. The rate of this process can be enhanced through heating it up to higher temperature.

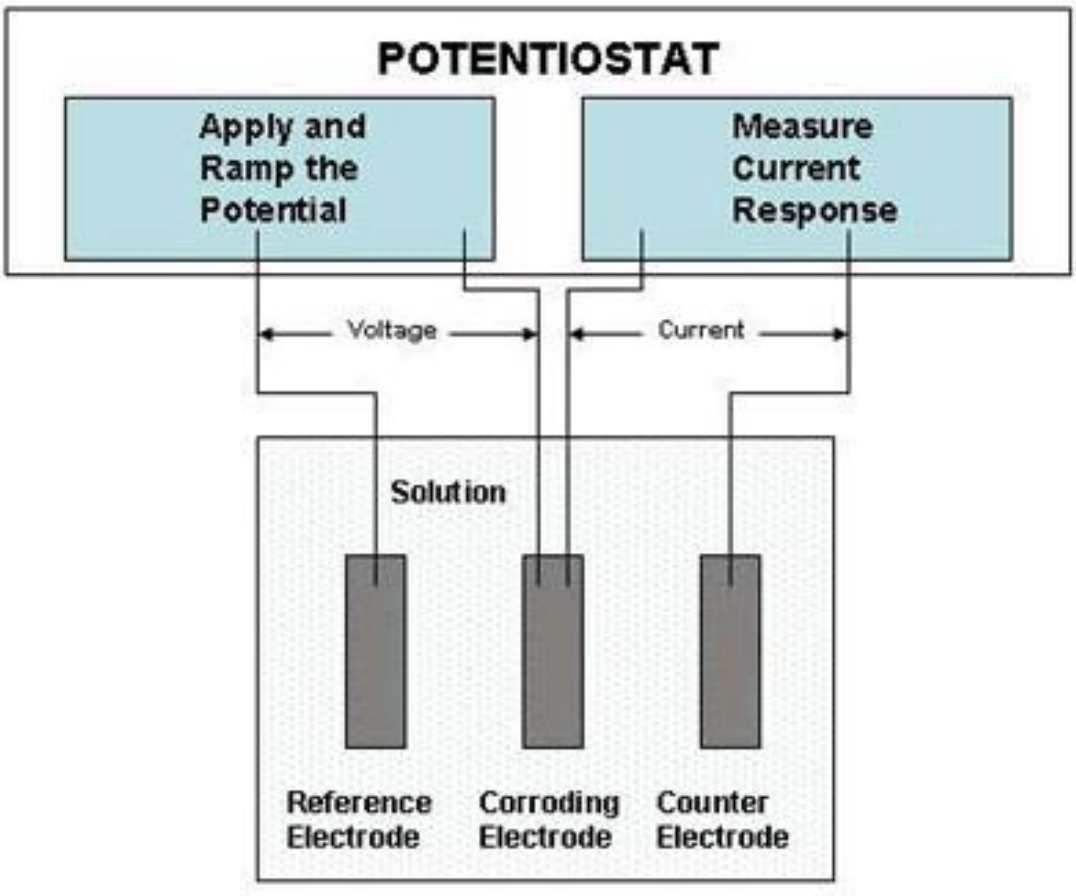

Figure 17.) The set-up of the potentiostat used for electro-deposition

The whole set-up of the potentiostat is visualized in figure 15. Typical potentiostat consists of three parts: reference electrode, corroding electrodes and counter electrode. The whole process of the fabrication of ZnO nanorods can be visualized in figure 16. The $Zn(NO_3)_2$ powders of calculated amounts were first dissolved into water to give $Zn(NO_3)_2$ solutions. The solution produced was then subjected to the hot-plate with stirring. The ITO/PET was then connected to AgCl and dipped into the $Zn(NO_3)_2$ electrolyte. After that, the whole set-up was heated up to 80°C with the hot-plate. When the whole set-up was stabilized at around 80°C, the potentiostat was switched on to start the electrodeposition process with different deposition times. After a certain minutes, ZnOH was obtained, and the ITO surface was rinsed with DI water to clear unwanted electrolyte. Finally, the thin film obtained was heated in the oven in order to ensure all the materials obtained are feasibly converted to ZnO.

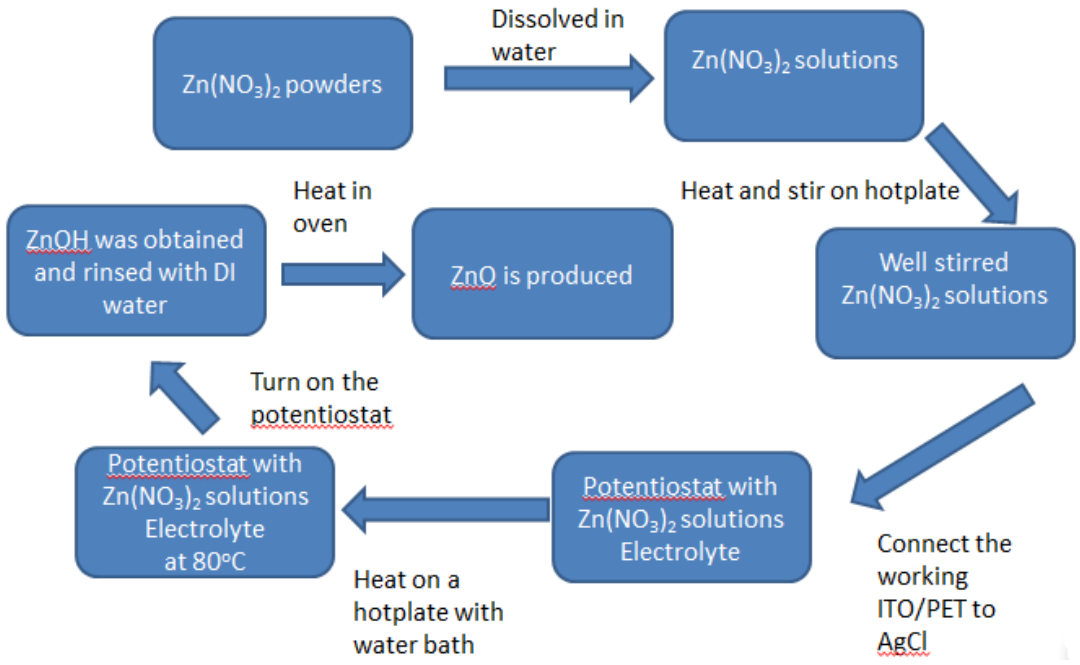

Figure 18.) Experimental process of the ZnO processing

3.2 Trials of synthesis

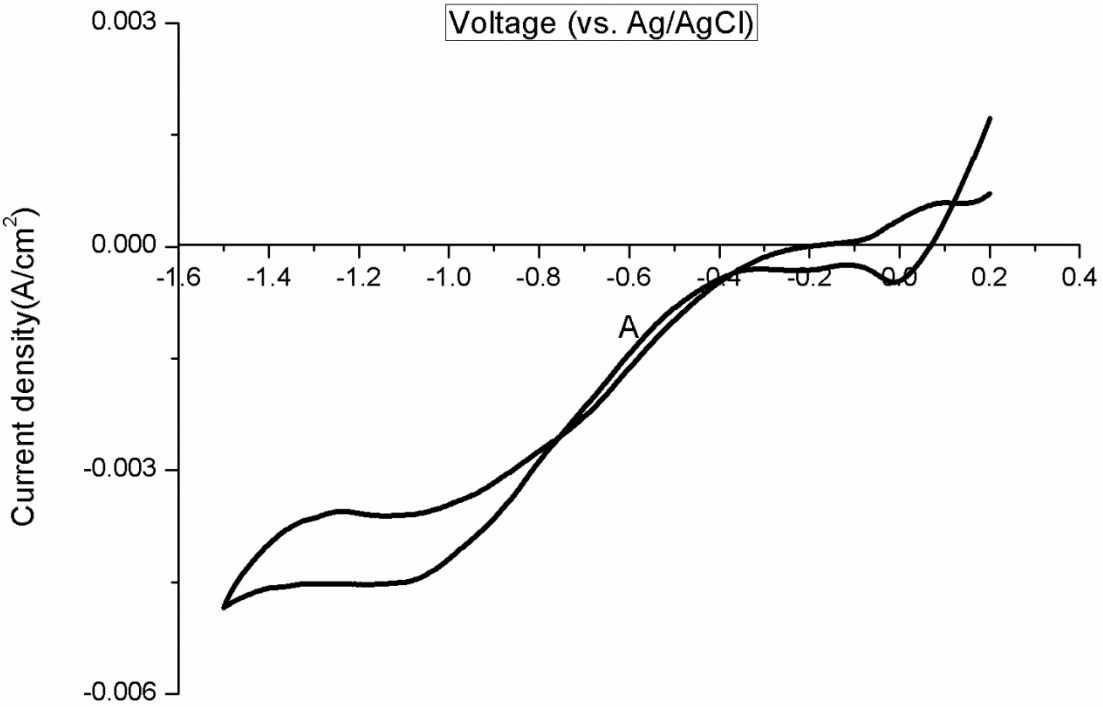

Figure 19.) Cyclic voltammogram of ITO coated PET electrode in 0.01M zinc nitrate solution with water bath temperature 80^{o}C and the pH value is 7

Before the trial start, a cyclic voltammorgram was applied to see what applied voltage should be used in the reaction. Figure 17 shows the scan from 0.2V to above -1.5V in the zinc nitrate solution. A steep increment of cathodic current between -0.4 V to -1.5 V was observed. The cathodic current reached 4.5 mA at about -1.2V. Within that region, the reduction of the nitrate ions and hydrogen ions resulted in a large increase in cathodic current due to their similarity in reducing potentials. The generation of hydroxide ions helps the formation of zinc oxide which is from the reduction of nitrate ions. The reduction follows the equation as follows

$$NO_3^- + Zn^{2+} + 2e^- \rightarrow ZnO + NO_2^-$$

When the potential further decreased beyond -1.2V, only a slight increment of the cathodic current was observed. This further increase in the cathodic current may be attributed to a more negative potential which favors the reduction process of the zinc metal on the substrate surface, and this leads to a large generation of current flow. However, for too high cathodic voltage, multi-reactions like electrodeposition of zinc metal are of higher probability to be occurred. Besides, the cross point of the cyclic voltammorgrams refers to the potential of the formation of nucleation. From the cyclic voltammorgras provided before, it showed that the nucleation of ZnO started at -0.7V. Therefore, the voltage ranges for electrodeposition of ZnO should be between -0.7V to -.1.2V.

3.2.1 Variation of cathodic voltage in the fabrication of ZnO nanorods

Variation of applied cathodic voltage induces changes of characteristic as well as morphology of the ZnO nanorods. In order to study the effects of the cathodic voltage on the properties of ZnO nanorods, fabrication parameters such as cathodic voltages between 0.9 V and 1.5 V, deposition time fixed at 5 min, temperature at 80 ^{o}C, reaction area of 6 cm^3 and concentration of $Zn(NO_3)_2$ at 0.03M were employed. Table 2 shows the name of the samples and their fabrication parameters.

Table 2.) ZnO nanorods produced using potentiostat with the variation of cathodic voltage while other factors remain

Samples	Time (mins)	Applied Voltage(-V)	Temperature (^{o}C)	Reaction area(cm^3)	Concentration of $Zn(NO_3)_2$
ZnO_1	5	0.9	80	6	0.03M

ZnO_2	5	1.0	80	6	0.03M
ZnO_3	5	1.1	80	6	0.03M
ZnO_4	5	1.2	80	6	0.03M
ZnO_5	5	1.4	80	6	0.03M
ZnO_6	5	1.5	80	6	0.03M

3.2.2 Variation of concentration in the fabrication of ZnO nanorods

Similarly, different concentration of $Zn(NO_3)_2$ also induces changes of characteristic as well as morphology of the ZnO nanorods. In order to study the effects of concentration of $Zn(NO_3)_2$ on the properties of ZnO nanorods, fabrication parameters such as cathodic voltage fixed at 1.1 V, deposition time fixed at 5 min, temperature at 80 ^oC, reaction area of 6 cm^3 and concentration of $Zn(NO_3)_2$ between 0.03 M and 0.10 M were employed. Table 3 shows the name of the samples and their fabrication parameters

Table3.)ZnO nanorods produced using potentiostat with the variation of concentration while other factors remain

Samples	Time (mins)	Applied Voltage(-V)	Temperature (^oC)	Reaction area(cm^3)	Concentration of $Zn(NO_3)_2$
ZnO_7	5	1.1	80	6	0.03M
ZnO_8	5	1.1	80	6	0.05M
ZnO_9	5	1.1	80	6	0.06M
ZnO_10	5	1.1	80	6	0.08M
ZnO_11	5	1.1	80	6	0.09M
ZnO_12	5	1.1	80	6	0.10M

3.2.3 Variation of deposition time in the fabrication of ZnO nanorods

Different deposition time induces changes of characteristic as well as morphology of the ZnO nanorods. In order to study the effects of deposition time on the properties of ZnO nanorods, fabrication parameters such as cathodic voltage fixed at 1.3 V, deposition time varied between 5 min to 40 min, temperature at 80 ^{o}C, reaction area of 6 cm^3 and concentration of $Zn(NO_3)_2$ of 0.03 M were employed. Table 4 shows the name of the samples and their fabrication parameters.

Table4.)ZnO nanorods produced using potentiostat with the variation of deposition time while other factors remain

Samples	Time (mins)	Applied Voltage(-V)	Temperature (^{o}C)	Reaction area(cm^3)	Concentration of $Zn(NO_3)_2$
ZnO_13	5	1.3	80	6	0.03M
ZnO_14	10	1.3	80	6	0.03M
ZnO_15	15	1.3	80	6	0.03M
ZnO_16	20	1.3	80	6	0.03M
ZnO_17	30	1.3	80	6	0.03M
ZnO_18	40	1.3	80	6	0.03M

3.2.4 Variation of PH value in the fabrication of ZnO nanorods constant temperature 80^{o}C

Varying pH value of the solution induced characteristic changes and morphology. The samples of ZnO_19 to ZnO_24 were the samples with increasing pH values of the solution in order to study the effects of pH value on the properties of the ZnO nanorods film with specific features.

Table 5.)ZnO nanorods produced using potentiostat with the variation of pH value of the solution while other factors remain

Samples	Time (mins)	Applied Voltage(-V)	pH value	Reaction area(cm^3)	Concentration of $Zn(NO_3)_2$
ZnO_19	5	0.9	3.3	6	0.03M
ZnO_20	5	0.9	4.1	6	0.03M
ZnO_21	5	0.9	6.0	6	0.03M
ZnO_22	5	0.9	7.1	6	0.03M
ZnO_23	5	0.9	8.0	6	0.03M
ZnO_24	5	0.9	9.0	6	0.03M

3.2.5 Variation of applied voltage in the fabrication of Al-doped ZnO nanorods constant temperature 80°C and, neutral and acidic condition

In order to produce n-type ZnO nanorods, Al was doped into the ZnO. With a small portion of $Al(NO_3)_3$ of around 5 mol% was added to the $Zn(NO_3)_2$ solution. After that, the effects of the applied cathodic voltage on the characteristic changes and morphology changes of the Al-doped ZnO nanorodes were investigated. The samples of ZnO_25 to ZnO_30 were the samples with increasing cathodic voltage in order to produce a trend of ZnO nanorods film with specific features.

Figure 20.) Al-doped ZnO nanorods produced using potentiostat with the variation

of cathodic voltage while other factors remain at neutral condition

Samples	Time (mins)	Applied Voltage(-V)	Temperature (^{o}C)	Reaction area(cm^3)	Concentration of $Zn(NO_3)_2$
ZnO_25	5	1.1	80	6	0.03M
ZnO_26	5	1.2	80	6	0.03M
ZnO_27	5	1.3	80	6	0.03M
ZnO_28	5	1.4	80	6	0.03M
ZnO_29	5	1.5	80	6	0.03M
ZnO_30	5	1.6	80	6	0.03M

With a small portion of $Al(NO_3)_3$ of around 5% of the solution are added to the solution. Variation of applied cathodic voltage induced characteristic changes and morphology. The samples of ZnO_25 to ZnO_30 were the chosen samples subjected to increasing cathodic voltage in order to produce a trend of ZnO nanorods film with specific features.

Figure 21.) Al-doped ZnO nanorods produced using potentiostat with the variation of cathodic voltage while other factors remain at acidic condition

Samples	Time (mins)	Applied Voltage(-V)	Temperature (^{o}C)	Reaction area(cm^3)	Concentration of $Zn(NO_3)_2$
ZnO_31	5	1.1	80	6	0.03M
ZnO_32	5	1.2	79	6	0.03M
ZnO_33	5	1.3	80	6	0.03M
ZnO_34	5	1.4	78	6	0.03M
ZnO_35	5	1.5	78	6	0.03M
ZnO_36	5	1.6	79	6	0.03M

3.3 SEM spectrum of the Zinc Oxides ZnO obtained

The Scanning electron microscopy spectra are presented in the following figures. The following figures show the tendency of the formation of ZnO nanorods with different parameters such as the voltage applied on the potentiostat, the concentration of the solution, the pH value of the working electrolyte and the deposition time used for the deposition. The thickness of the deposited film due to different deposition time was also obtained by using SEM micrographs.

3.3.1 SEM of variation of cathodic voltage in the fabrication of ZnO nanorods

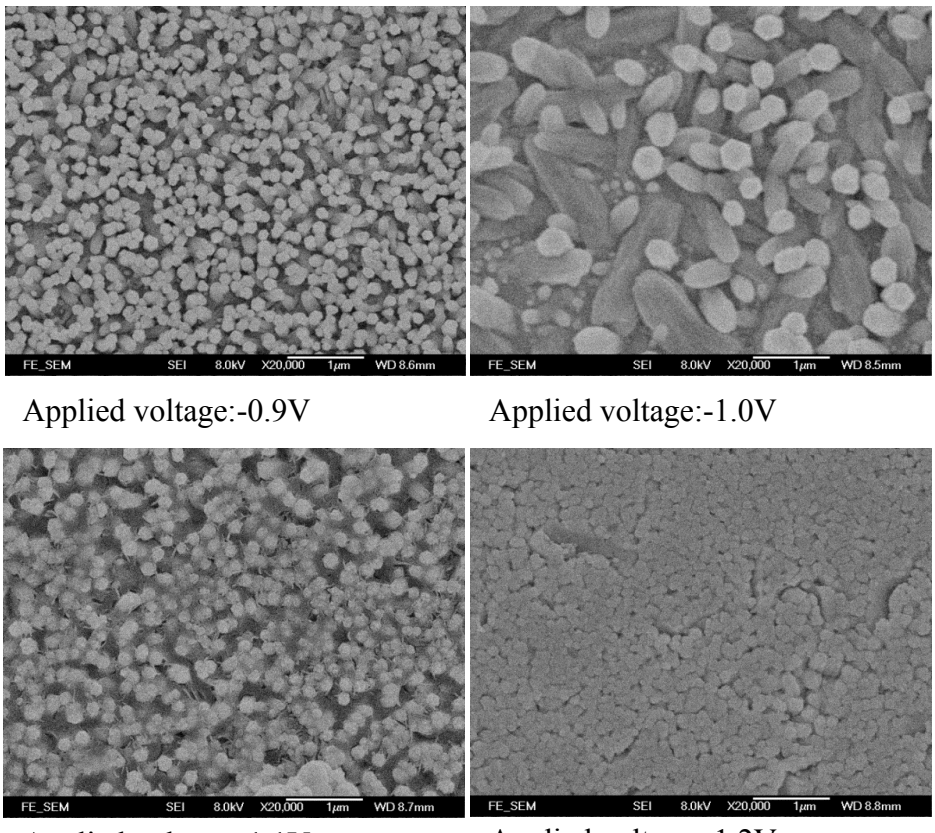

Applied voltage:-0.9V Applied voltage:-1.0V

Applied voltage:-1.1V Applied voltage:-1.2V

Figure 22.) SEM of variation of applied voltage in the fabrication of ZnO nanorods

Figure 22 summarizes the effects of applied voltage on the surface morphology of the ZnO fabricated films. Generally speaking, the applied voltage affects the sizes of the fabricated ZnO nanorods. As shown in Figure 22, a hexagonal shape indicating the existence of ZnO were observed in all micrographs. Furthermore, with increasing voltage, the packing density of the ZnO rods seemed to be increasing, indicating a higher deposition rate. Figure 21 shows the relationship between the applied voltage and the size of the ZnO nanorods. The average sizes of the ZnO produced in different applied voltages were 140 nm, 400 nm, 177 nm, 220 nm for applied voltages of -0.9 V, -1.0 V, -1.1 V and -1.2 V respectively. This indicates that the higher the applied voltage, the larger the ZnO nanorods obtained.

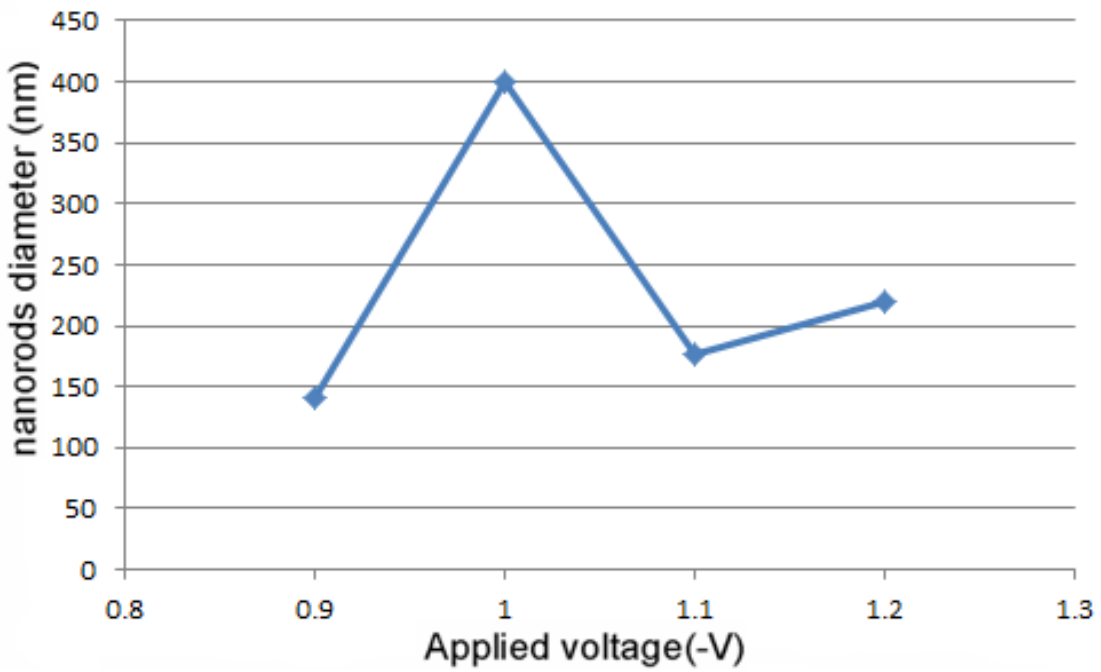

Figure 23.)Size of diameter of ZnO nanorods with respect to the applied voltage

3.3.2 SEM of variation of concentration of the $Zn(NO_3)_2$ solution in the fabrication of ZnO nanorods

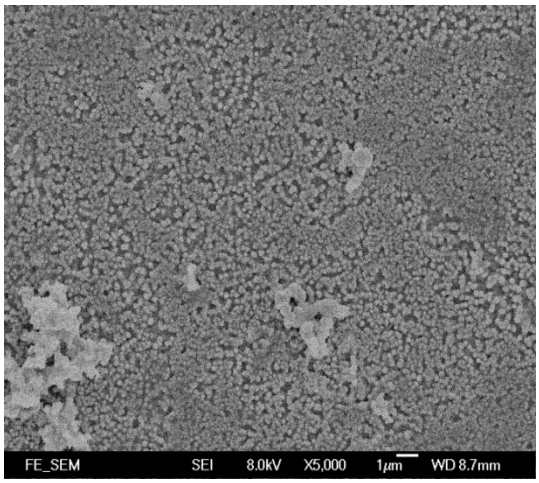

Concentration applied: 0.03M

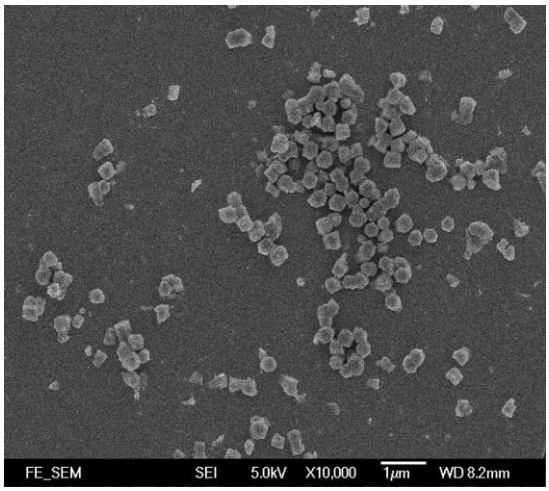

Concentration applied: 0.07M

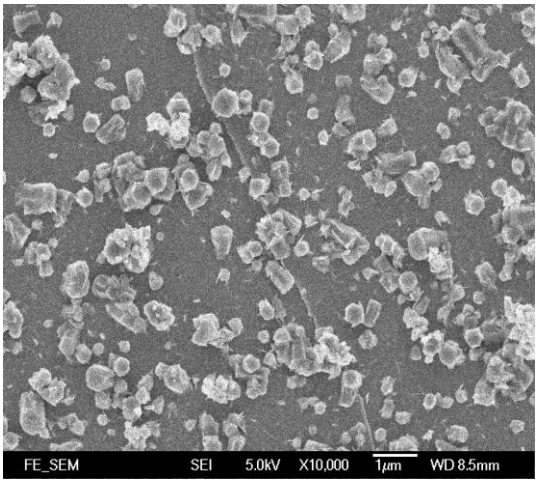

Concentration applied: 0.10M

Figure 24.) SEM of variation of concentration of the $Zn(NO_3)2$ solution in the fabrication of ZnO nanorods

Figure 24 shows the effects of concentration on the surface morphology of the ZnO fabricated films. Generally speaking, characteristic hexagonal shapes of ZnO rods were observed in all the samples. Furthermore, the $Zn(NO_3)_2$ solution concentration strongly affects the size as well as the packing density of the ZnO nanorods. Figure 25 shows

the relationship between the $Zn(NO_3)_2$ solution concentration and the size of the ZnO nanorods. The average sizes of the ZnO produced in different concentration were measured to be 250 nm, 317 nm and 533 nm as the concentrations were 0.03 M, 0.07 M and 0.10 M respectively. This means that the size of the diameters of ZnO increase with the decrease of the concentration of $Zn(NO_3)_2$ solution.

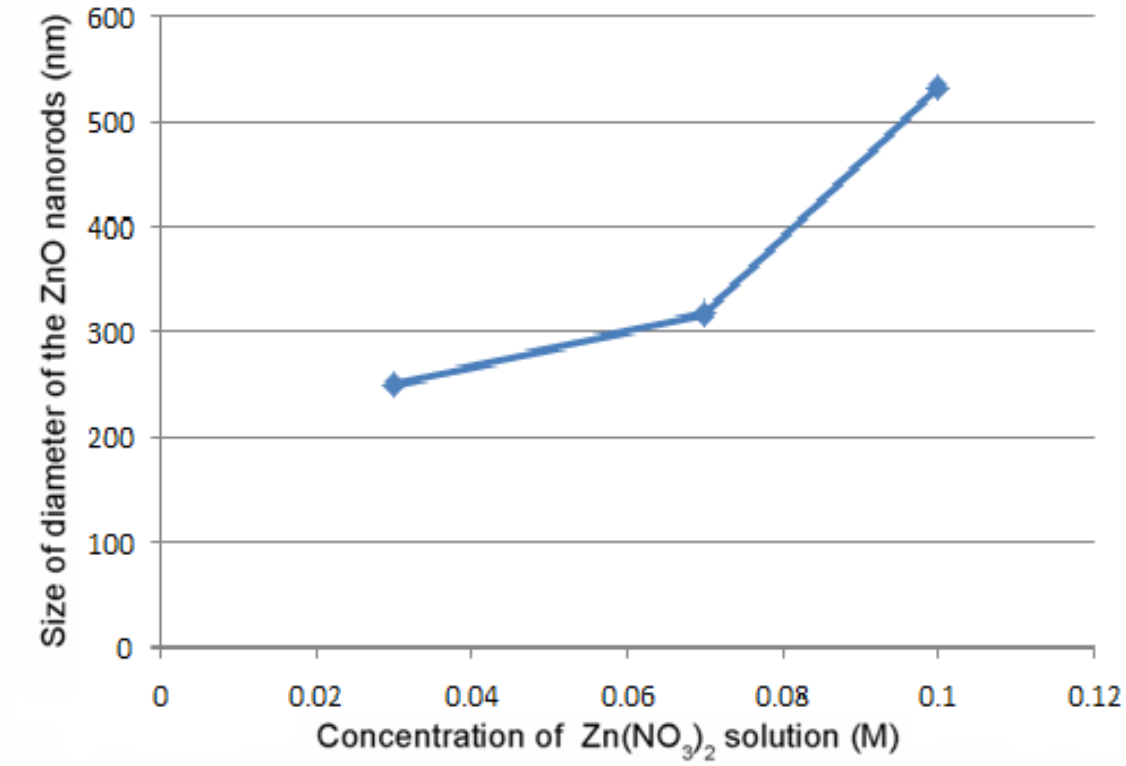

Figure 25.) Size of diameter of ZnO nanorods with respect to the concentration of $Zn(NO_3)_2$

3.3.3 SEM of variation of deposition time in the fabrication of ZnO nanorods

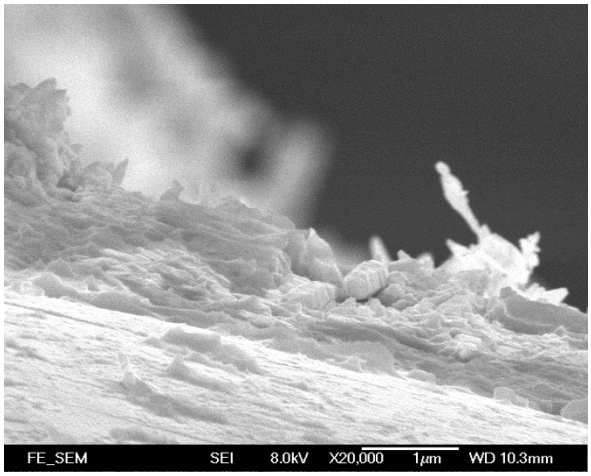

Deposition time: 15mins

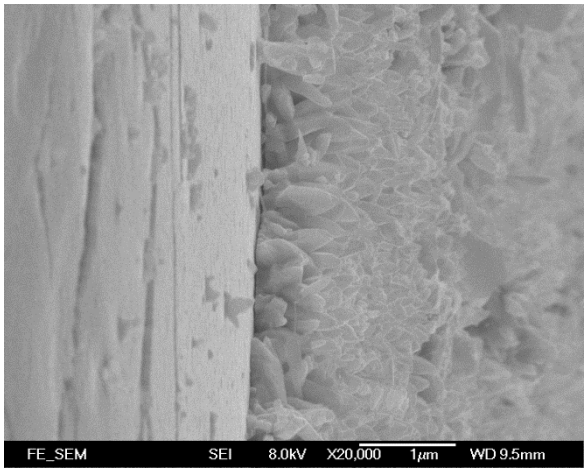

Deposition time:20 mins

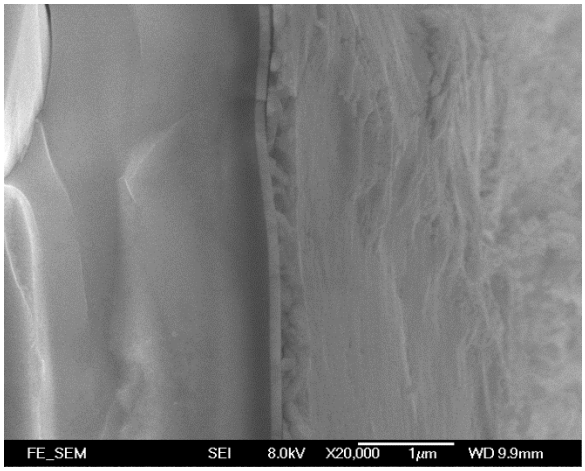

Deposition time:30 mins

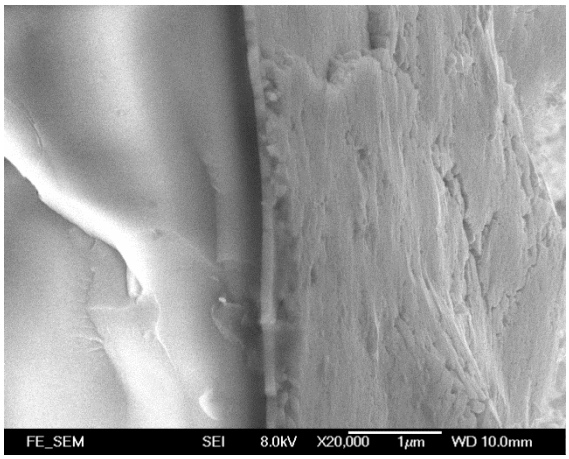

Deposition time:40 mins

Figure 26.) SEM of variation of deposition time in the fabrication of ZnO nanorods

Figure 26 shows the effects of the deposition time on the surface morphology of the ZnO fabricated films. Generally speaking, the length of the ZnO nanorods i.e. the thickness of the nanorods films depends on the deposition time. However, the average thicknesses of the ZnO films (or the lengths of the ZnO nanorods) were almost the same to be around 300nm for different deposition times at 15 mins, 20 mins, 30 mins and 40

mins. This may possibly due to the reduction in the intensity of electric field. When the the thickness of the ZnO increased with the deposition time, the conductivity working surface become very low and finally become almost insulating. Hence it is possible that when a certain thickness of ZnO is obtained from electrodeposition, the deposition process stopped.

3.3.4 SEM of variation of PH value in the fabrication of ZnO nanorods constant temperature

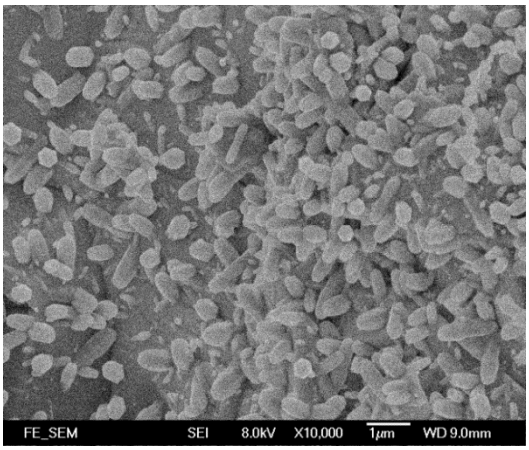

pH value: 4

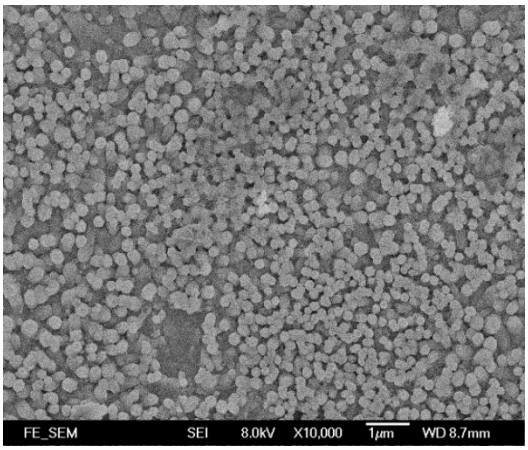

pH value: 5

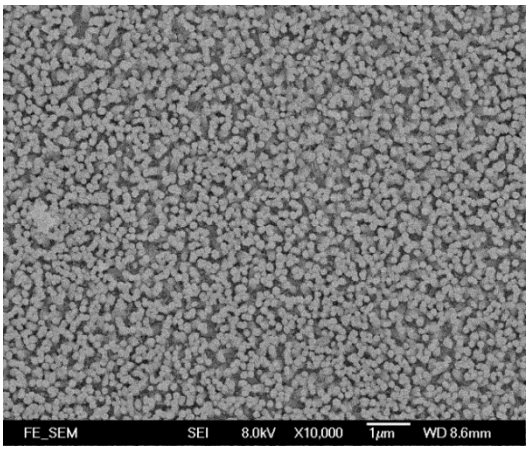

pH value: 7

Figure 27.) SEM of variation of pH value in the fabrication of ZnO nanorods constant temperature

Figure 27 demonstrates the effects of pH vlaue on the surface morphology of the ZnO fabricated films. Generally speaking, characteristic hexagonal shapes of ZnO rods were observed in all the samples. Again, ZnO nanorods of various sizes and the packing density of the films were largely related to the pH value. Indeed, the sizes as well as the packing density of the ZnO rods were increased with the pH value. However, if the pH value is less than pH 4, ZnO nanorods were not observed. Similarly, if the pH value was larger than 8, no ZnO nanorods were formed on top of the ITO glass substrates, indicating than the only possible pH window to form ZnO nanorods is between 4 to 8.

3.3.5 SEM of variation of applied voltage in the fabrication of Al-doped ZnO nanorods constant temperature and neutral condition

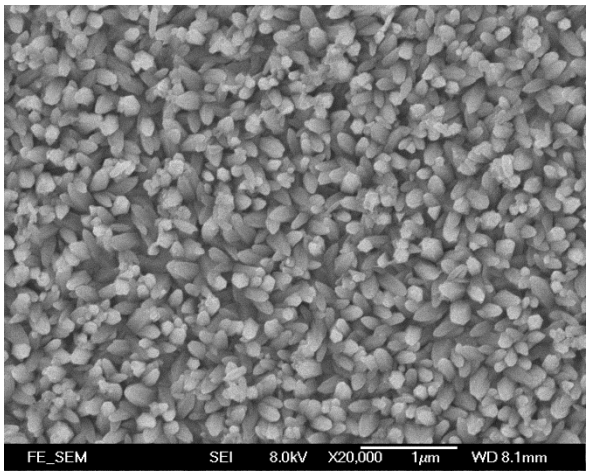

Applied voltage: -1.3V

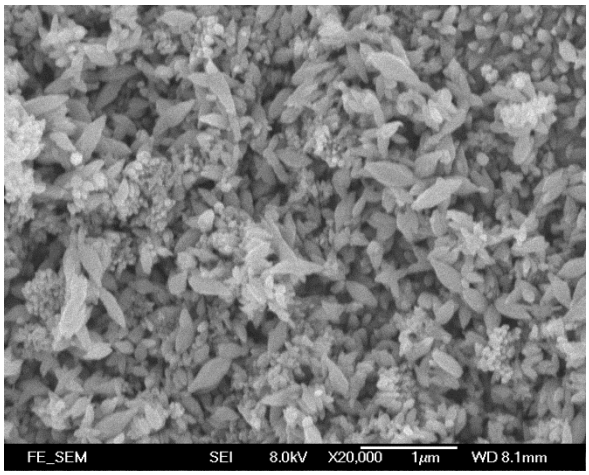

Applied voltage: -1.4V

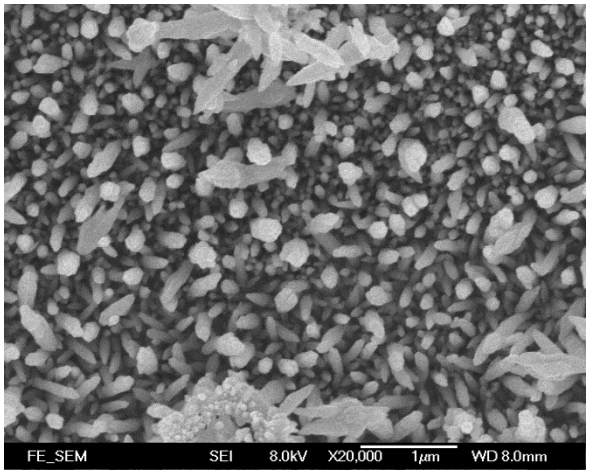

Applied voltage: -1.5V

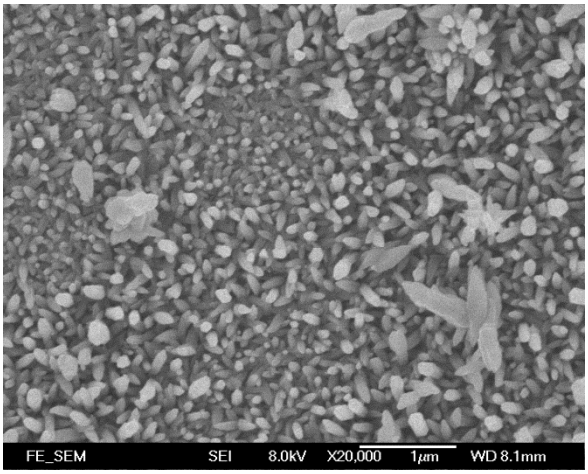

Applied voltage: -1.6V

Figure 28.) SEM of variation of applied voltage in the fabrication of Al-doped ZnO nanorods constant temperature and neutral condition

3.3.6 SEM of variation of applied voltage in the fabrication of Al-doped ZnO nanorods constant temperature and neutral condition

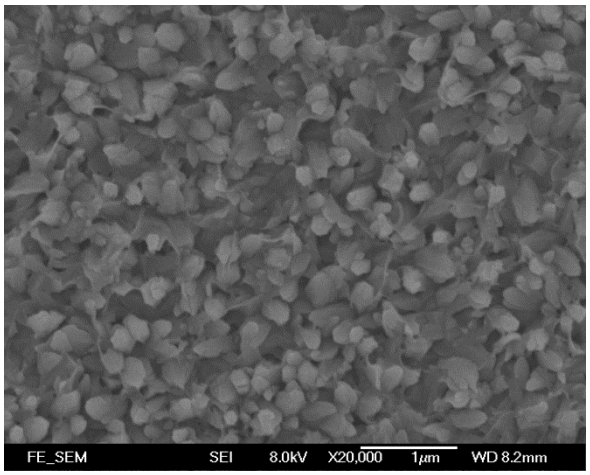

Applied voltage: -1.3V

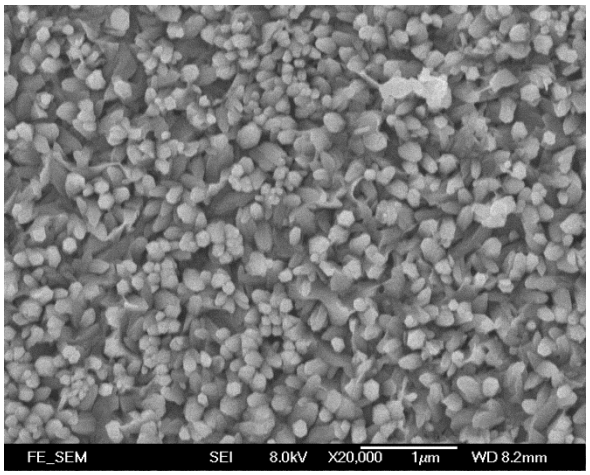

Applied voltage: -1.4V

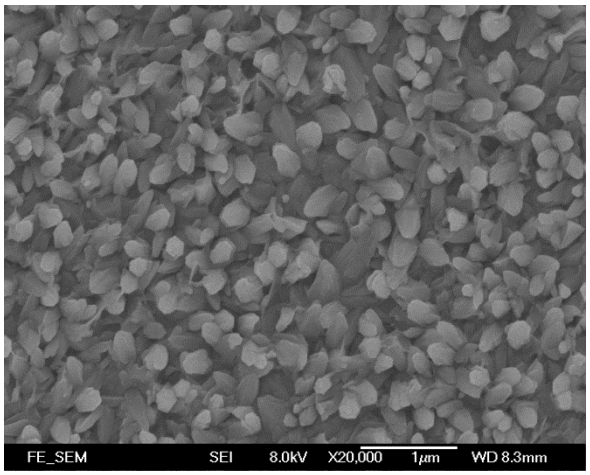

Applied voltage: -1.5V

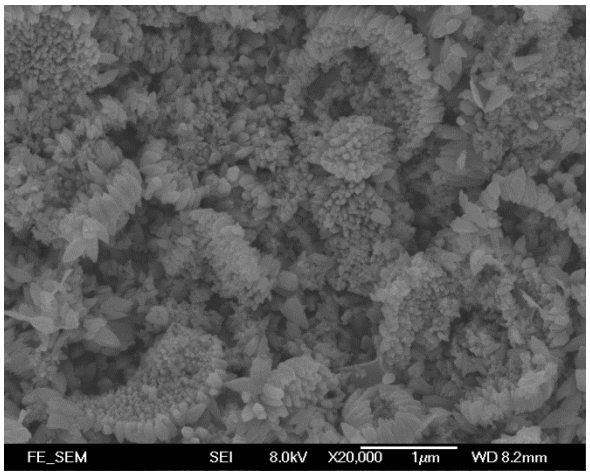

Applied voltage: -1.6V

Figure 29.) SEM of variation of applied voltage in the fabrication of Al-doped ZnO nanorods constant temperature and acidic condition

With the dopants of Al ions, the formation of the Al/ZnO nanorods is slightly deviated and the morphology has changed. Although the morphology of ZnO nanorod is slightly deviated, it still shows hexagonal shaped. Since, the shaped of ZnO under the SEM shows hexagonal shaped which is a specific feature, these samples can also be treated as ZnO.

3.4 X-ray diffraction pattern of ZnO

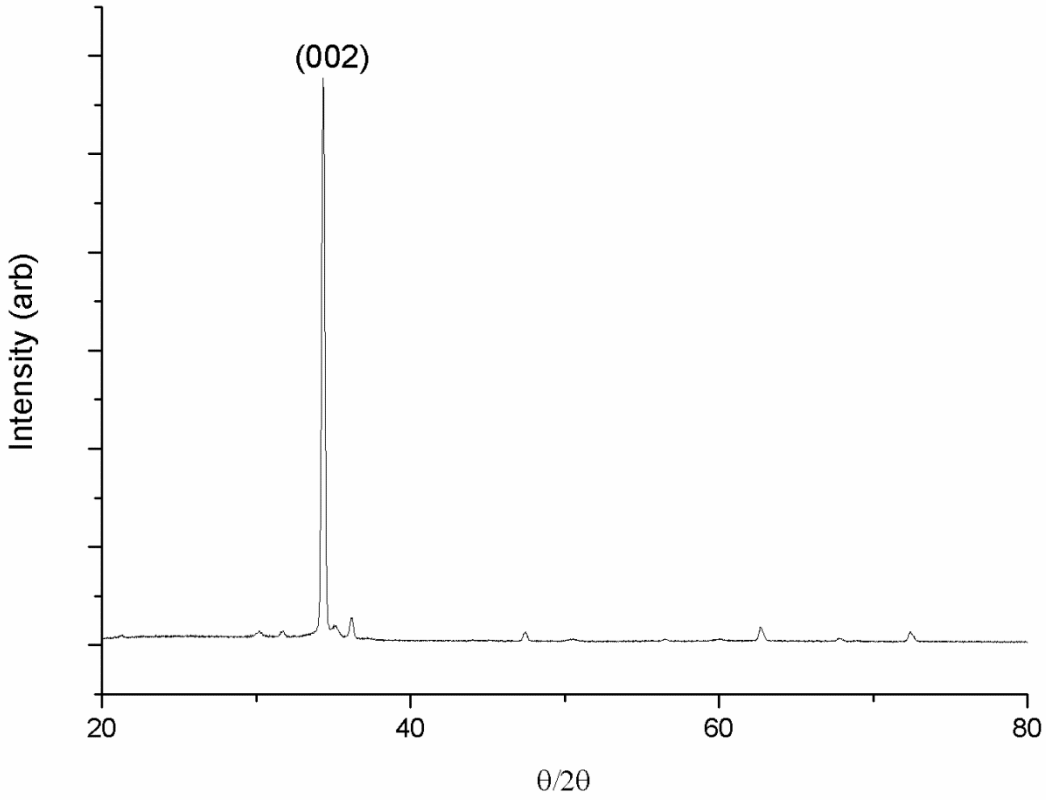

Figure 30.) X-ray diffraction pattern of ZnO showing a miller index of (002) peak at 80^{o}C, 0.03M and pH5

Figure 30 shows the θ-2θ scan of the ZnO nanorods films with the fabrication parameters of temperature of 80 °C, solution concentration of 0.03 M Ph value of 5. In the pattern, a sharp peak located at 34.3^{o} corresponding to miller index ZnO (002) was observed. The single (002) peak indicated that the nanorods obtained are almost in one direction i.e. evidence of the formation of 1D nanorods. Besides, from the calculation of Scherrers equation, the size diameters of the nanorods are of about 65 nm.

Chapter 4 Fabrication and Characterization of Copper Zinc Tin Sulfide (CZTS)

4.1 Introduction to experimental set-up

CZTS (Cu_2ZnSnS_4) nanoparticles were synthesized by hydrothermal process. The precursors $CuCl_2 \cdot 2H_2O$, $ZnCl_2 \cdot 6H_2O$, $SnCl_2 \cdot 5H_2O$, thiourea and oleyamine, of various molecular ratios were mixed to form a homogeneous aqueous solution as shown in figure 31.

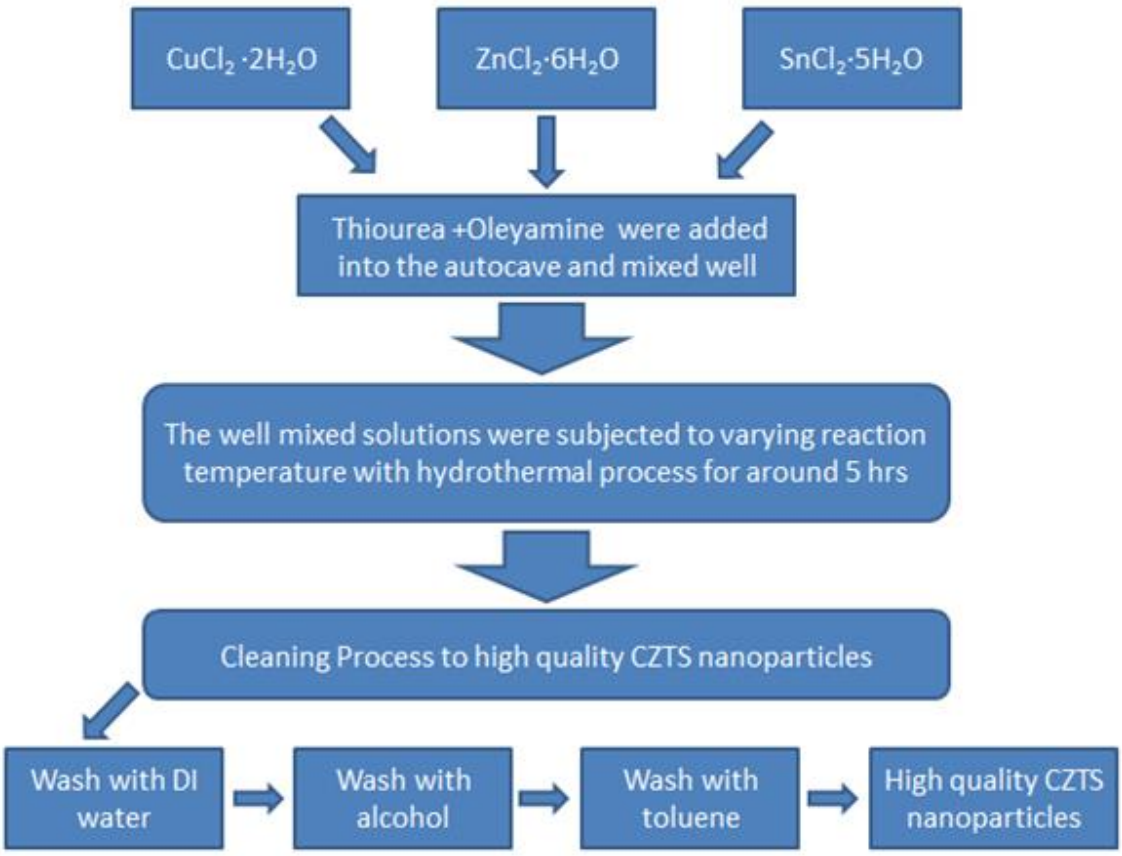

Figure 31.) Schematic diagram showing the hydrothermal process of the CZTS nanoparticles.

After stirring vigorously for 1 hr, the solution was transferred to a 50ml Teflon-

lined stainless autoclave. The mixture was sealed and allowed to heat at various temperatures (130-180^{o}C) for 5 hrs under autogenous pressure. After cooling, the powders were centrifuged, washed several times in sequence with deionized water, toluene and alcohol to remove the impurities and unwanted organic byproducts.

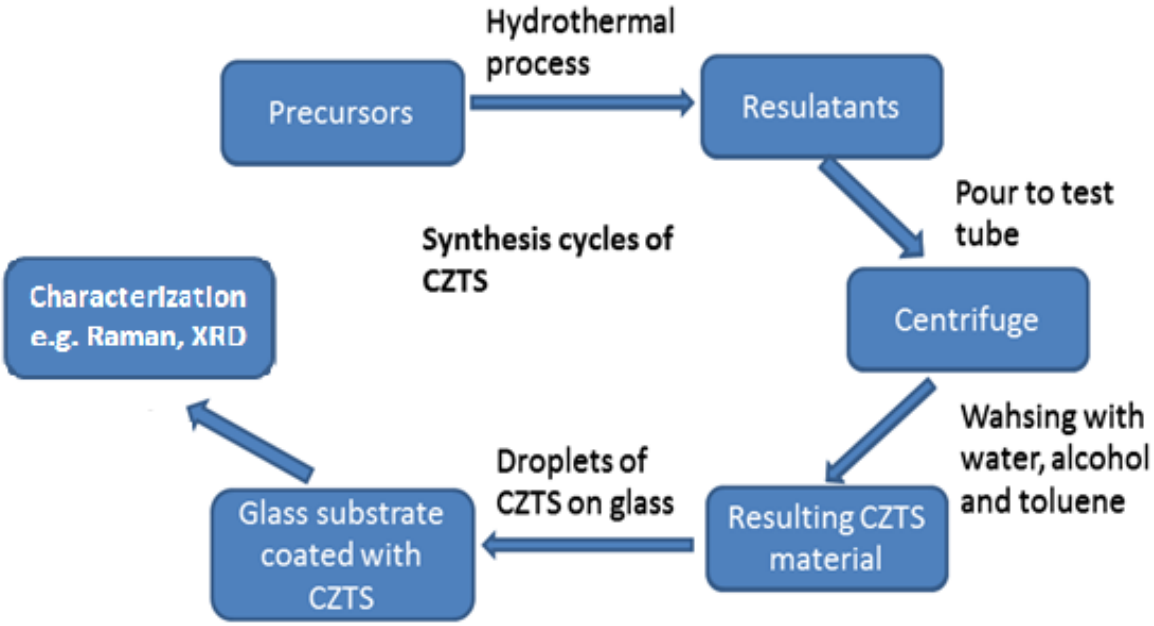

Figure 32.) The synthesis cycles of CZTS nanoparticles

The advantages of the hydrothermal method for synthesizing nanocrystals are low reaction temperature, environmental friendliness and precise control of composition. In the process for synthesizing CZTS nanocrystals, non-toxic $Sn(II)Cl_2$, $Cu(CH_3COO)_2$ and $Zn(NO_3)_2$ were dissolved in mixed solution of DI-water and ethylenediamine under stirring. Then, thiourea (CSN_2H_4) was added drop by drop to form the final precursor.

After fabrication, all the precursors are cheap and abundant. Furthermore, they are environmental friendly and non-toxic. The CZTS crystal structure was studied by x-

ray diffractometer (XRD, Philips x'pert system) with CuKα radiation operated at an acceleration voltage of 50kV. Raman spectra were taken using 488nm laser line of an air cooled Ar-ion laser. A microscope was used to focus the incident laser beam to a spot of 100μm in diameter. Raman specta were recorded by a 100x lens system in back scattering geometry. The size and shape of the obtained CZTS nanocrystals were studied by the transmission electron microscope (TEM, JEOL JEM 2010). The PL measurements which were carried out at room temperature, A Xenon lamp (Xe 900) with excitation source at 750nm was employed in the PL measurements.

4.2 The effects of the precursor composition on the structural properties of CZTS nanopowders

The precursors materials $CuCl_2 \cdot 2H_2O$, $ZnCl_2 \cdot 6H_2O$, $SnCl_2 \cdot 5H_2O$, and thiourea of 0.01M concentration were prepared for the ease of comparison.

Table 6.) CZTS powders with various composition ratios of Cu:Zn:Sn:S

Samples	$CuCl_2 \cdot 2H_2O$/ ml	$ZnCl_2 \cdot 6H_2O$/ ml	$SnCl_2 \cdot 5H_2O$/ ml	Thiourea/ Ml	Ratio obtained from EDX
CZTS a	6	3	3	12	2:0.82:1.08:1.89
CZTS b	6	3	3	15	2:0.84:1.13:2.31
CZTS c	6	3	3	18	2:0.76:0.97:1.98
CZTS d	6	3	3	21	2:0.78:1.02:2.74
CZTS e	6	3	3	24	2:0.78:1.6:3.69
CZTS f	6	3	3	27	2:0.81:1.06:4.32
CZTS g	6	3	3	30	2:0.84:1.04:4.49
CZTS h	6	6	3	27	2:0.78:1.04:4.35
CZTS i	6	9	3	27	2:0.79:0.96:4.21
CZTS j	6	12	3	27	2:0.84:0.95:4.02
CZTS k	6	15	3	27	2:0.95:0.98:3.89
CZTS l	6	18	3	27	2:0.9:0.78:3.99

CZTS has a chemical formula of Cu_2ZnSnS_4, indicating that the ratio of Cu:Zn:Sn:S should be 2:1:1:4. Table 6 shows the Cu:Zn:Sn:S ratio obtained from EDX measurement. For sample CZTS-a using the 2:1:1:4 stoichiometric ratio of precursor in the fabrication, large deviation of the product's stoichiometric ratio was observed a large amount of sulfur as well as small amount of Zn were missing i.e. using the stoichiometric amount of the precursors, the samples show a lack of zinc and sulfur source. In order to obtain CZTS samples of correct stoichiometric ratio, various

amounts of excess $ZnCl_2$ as well as thiourea were used in the fabrication.

4.3 X-ray diffraction pattern of CZTS

The CZTS crystal structure was studied by x-ray diffractometer (XRD, Philips x'pert system) with CuKα radiation operated at an acceleration voltage of 50kV.

4.3.1X-ray diffraction pattern of CZTS in different temperature

Fig. 33 shows the XRD patterns of the synthesized CZTS particles of various hydrothermal temperatures. The composition of the precursors used was 2:5:1:9. The obtained XRD patterns matched well with the XRD pattern reported by Lu et al. [10]. In the XRD spectra, peaks due to impurities such as Cu_3SnS_4, CuS, SnS and SnS_2 were not observed in our samples. However, the diffraction peaks of impurity Cu_2SnS_3 (CTS) are very close to those of CZTS for example, the CZTS (112), CZTS (200) and CZTS (220) overlapped with CTS (121), CTS (411) and CTS (620), and cannot be differentiated by using XRD. Thus Raman spectroscopy was employed to demonstrate that the nanoparticles were of pure CZTS form without CTS impurity. On the basis of our XRD data, the cystallinities of the CZTS nanoparticles fabricated at 130^{o}C, 150^{o}C and 180^{o}C were found to be 67%, 81% and 91% respectively. The grain size of the nanoparticles fabricated was estimated using Scherrer Equation. In the calculation, the line width of the CZTS (112) peak was used in the equation because of its strong intensity. The estimated grain size was found to be9nm, 10nm, 12nm for particles fabricated at 130^{o}C, 150^{o}C, 180^{o}C respectively.

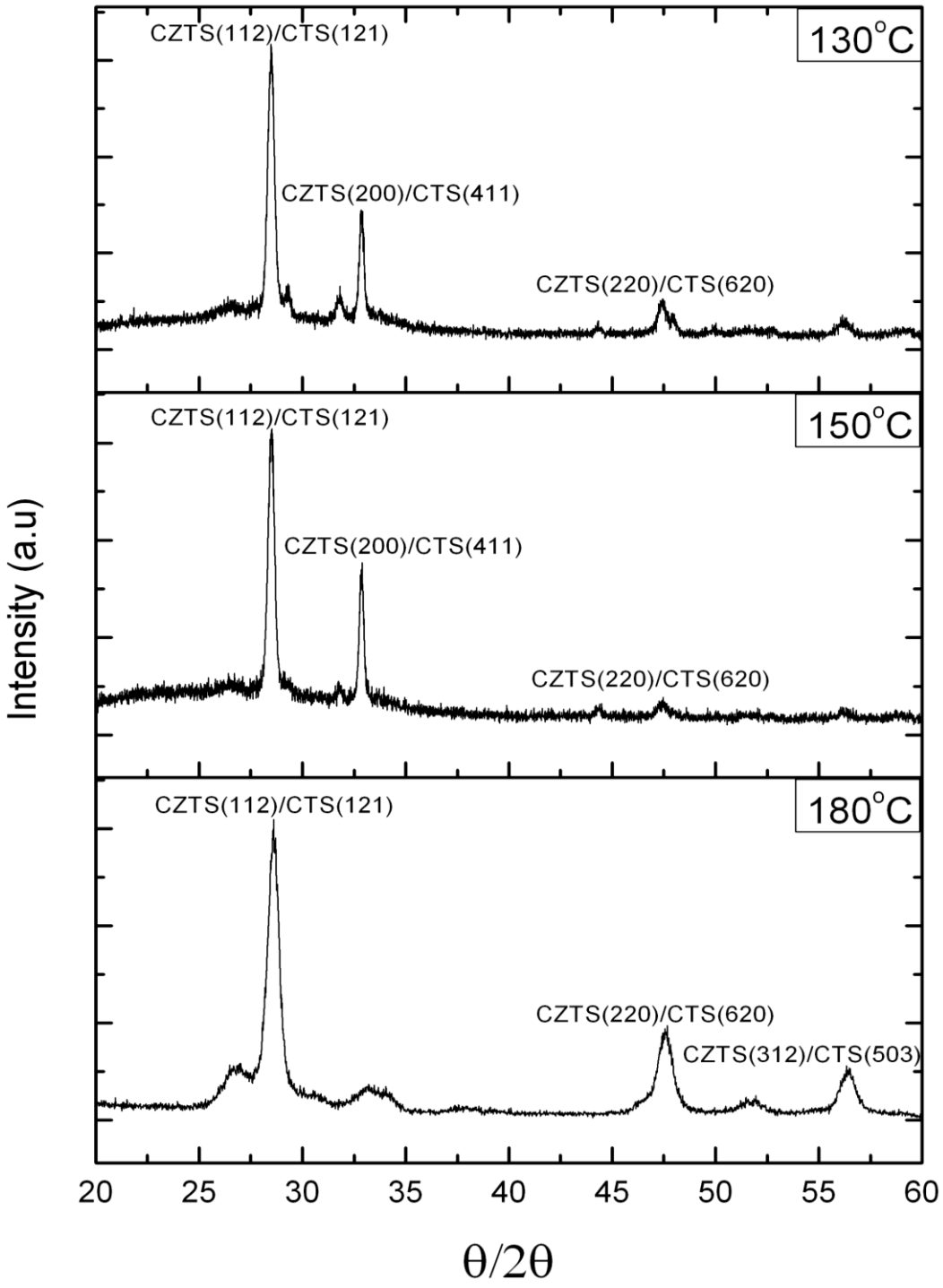

Figure 33.) XRD of CZTS nanoparticles obtained from 130°C, 150°C and 180°C respectively.

4.3.2X-ray diffraction pattern of CZTS in different processing time

Figure34, the XRD scan through 20^{o} to 65^{o} with four different reacting time of 8 hrs, 24 hrs, 32 hrs and 42 hrs. The unwanted phase which possibly generated by the ZnS located in 26^{o} is decreased as the reaction time increased.

Besides, the intensity of the peaks also increased with the increased in processing time which may possibly due to the increased in the crystallinity. Since there is sufficient time for the CZTS particles to be tightly bonded and grew in a more uniform direction, so that the intensity of the peaks are strengthen. However, it is also trivial that, the peaks obtained become narrower with the increased in the processing time. This may possibly due to the agglomeration of the CZTS nanoparticles since the smaller is the particles the broader is the peaks. Hence, it is crucial to choose the processing time to obtain CZTS nanoparticles of specific size range.

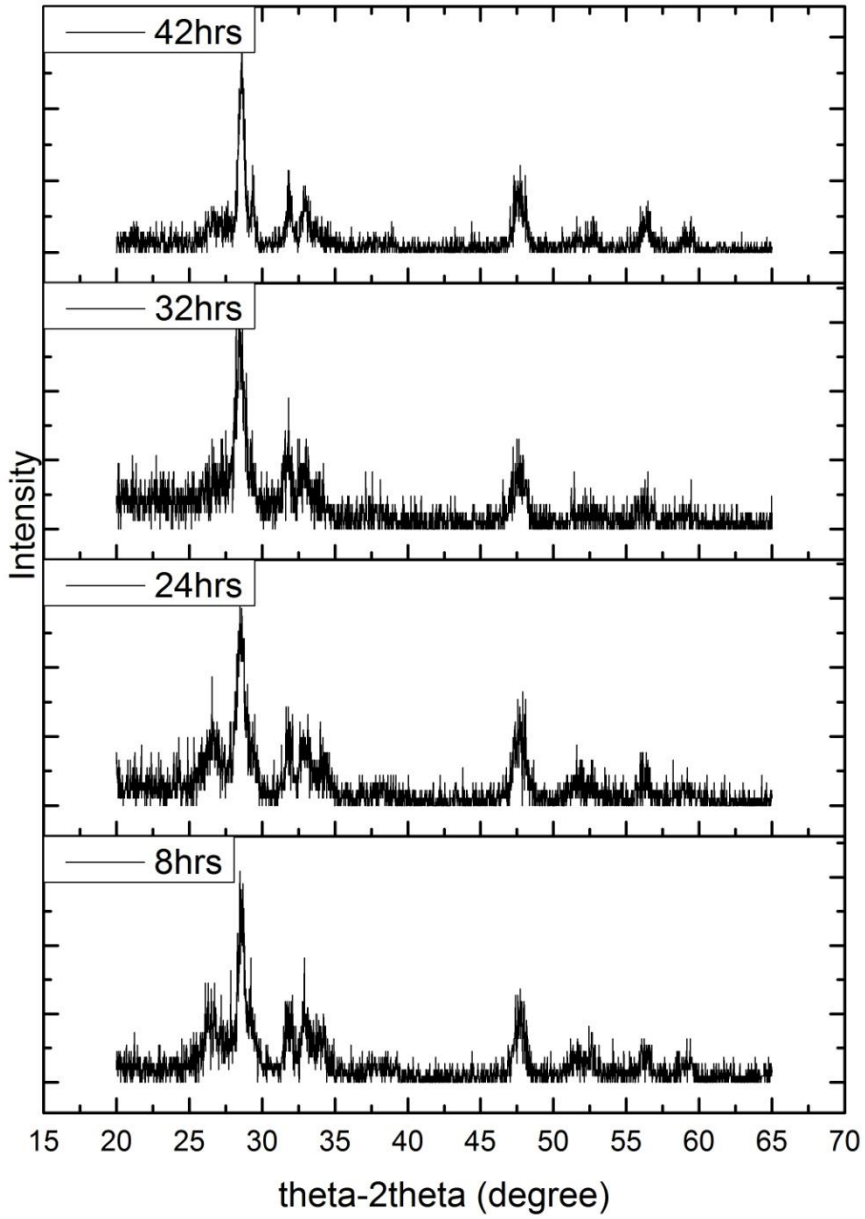

Figure 34.) XRD of CZTS in different processing time, 8hrs, 24 hrs, 32 hrs, 42 hrs.

4.4 Raman spectra of CZTS Nanoparticles

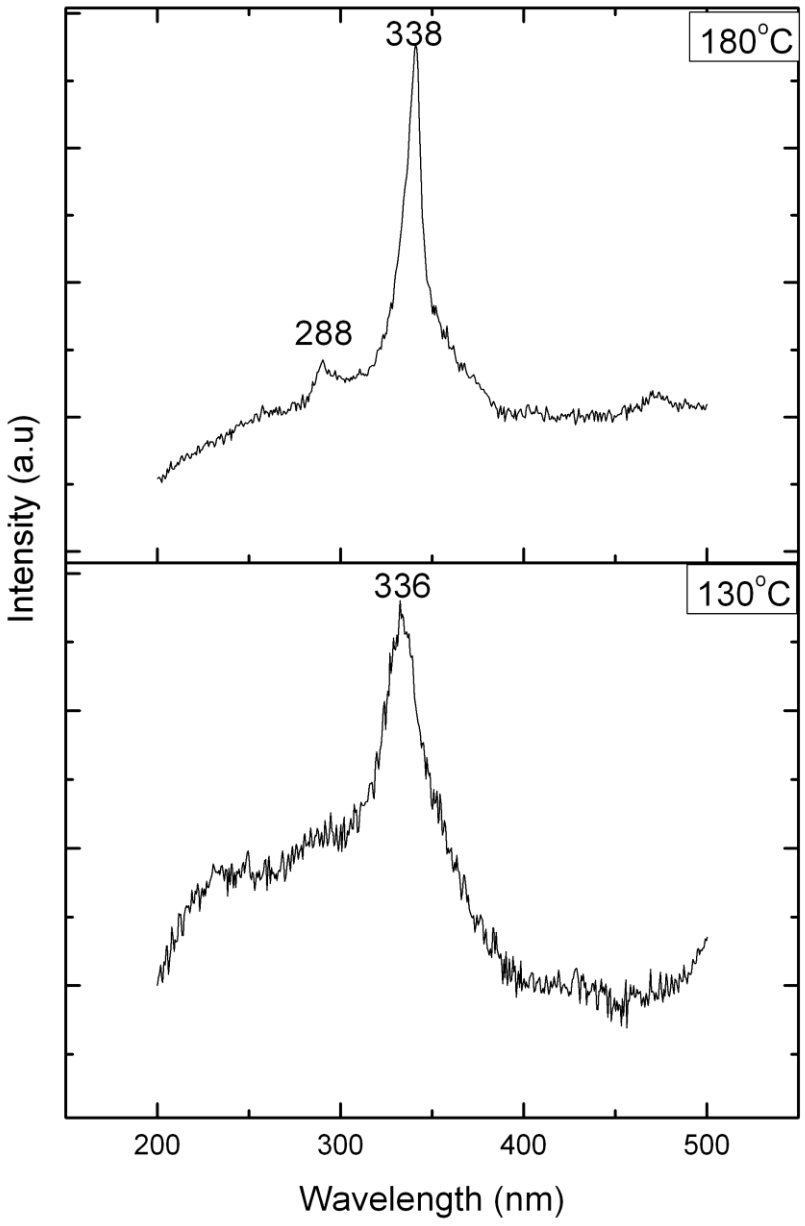

Figure 35.)Raman peaks of CZTS of 130 ^{o}C and 180 ^{o}C respectively

Raman spectra of CZTS obtained by Himmrich et al. [94] showed a strong peak at 336cm^{-1} and two weak peaks at 285 cm^{-1} and 362 cm^{-1} respectively. On the other hand, Fernandes [95] reported that the Raman spectrum of CTS contains strong peak at 298cm^{-1} and another one at 356cm^{-1}.

Fig. 35 shows the the Raman spectra of the CZTS nanoparticles synthesized at two different temperatures. The two spectra contained similar features i.e. a strong peak and a weak peak. The most significant peak found was at~ 338cm^{-1} indicating the existence of CZTS. Besides, the 338cm^{-1} peak had a broad shoulder on the low energy side and this might be paritially due to the weak 288cm^{-1} peak of the CZTS phase. Comparing the two figures, the full-width at half- maximum of the nanoparticles fabricated at 180^{o}C (11cm^{-1}) was much smaller than that of nanoparticles fabricated at 130^{o}C(21cm^{-1}). This indicates a better crystallinity of the nanoparticles fabricated at higher temperature, and this is consistent with XRD data. Futhermore, the intensity of the sample fabricated at 180^{o}C was stronger with a better signal to noise ratio. As a result, the other weak 288cm^{-1} peak of the CZTS was also observed.

4.5 SEM obtained from CZTS nanoparticles

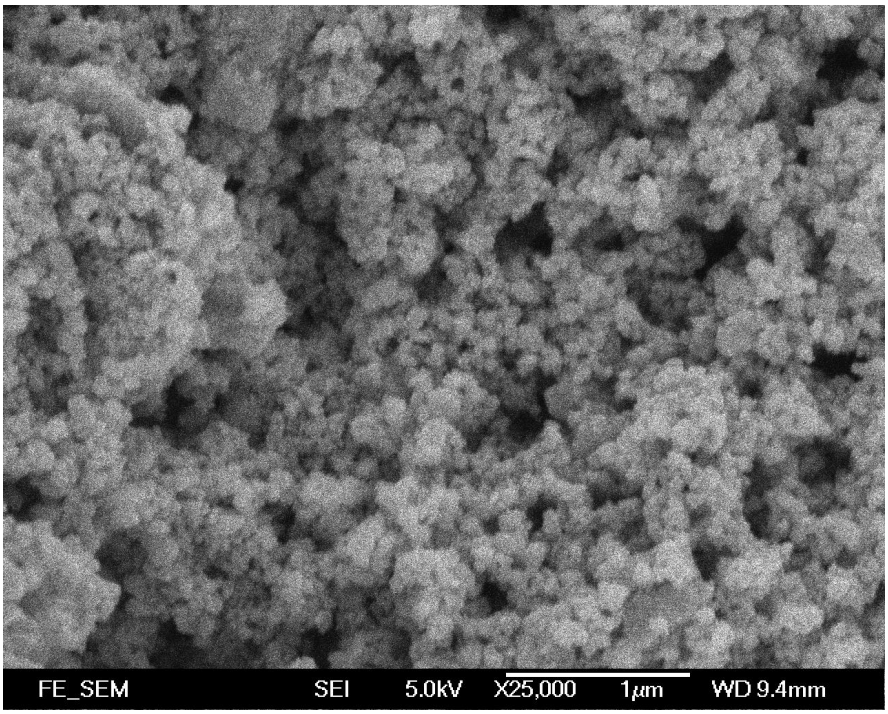

Figure 36.) SEM of CZTS nanoparticles

4.6 TEM obtained from CZTS nanoparticles

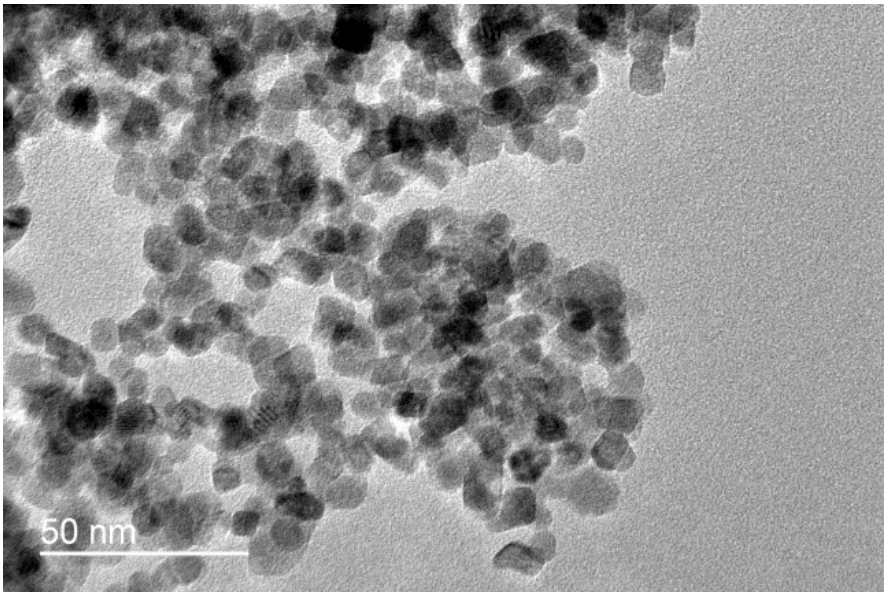

Figure 37.) TEM of CZTS nanoparticles

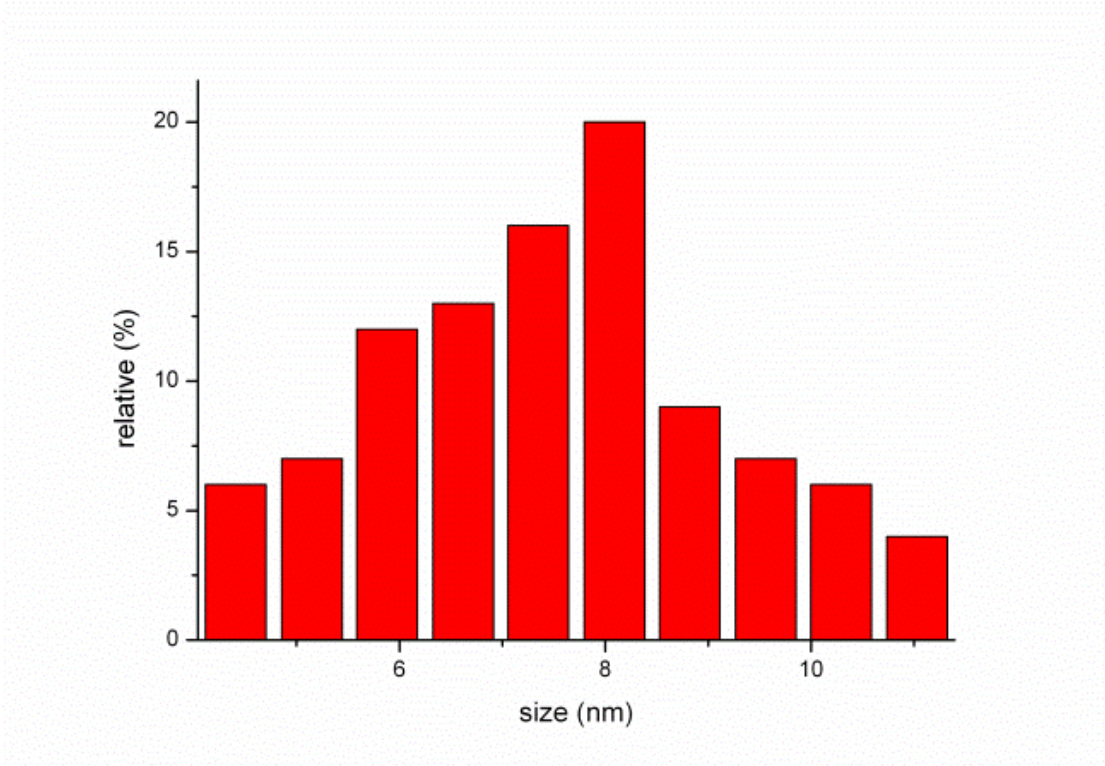

Figure 38.) Size distribution of CZTS nanoparticles

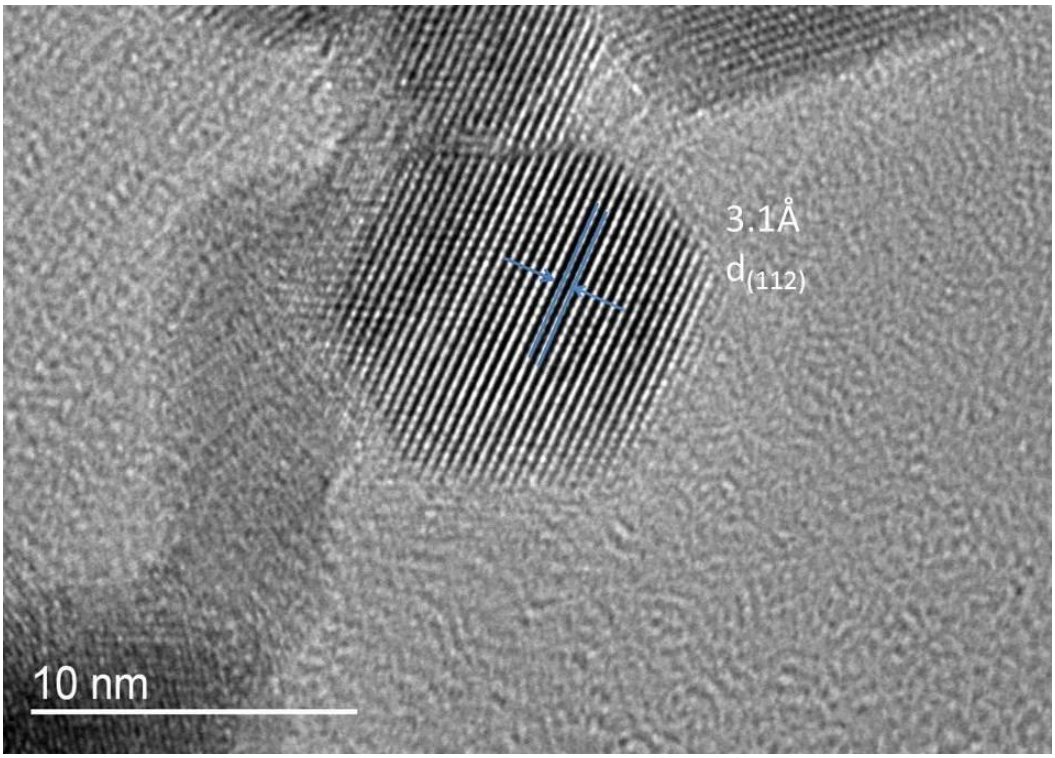

Figure 39.) High Resolution Transmission Electron Microscopy (HRTEM)

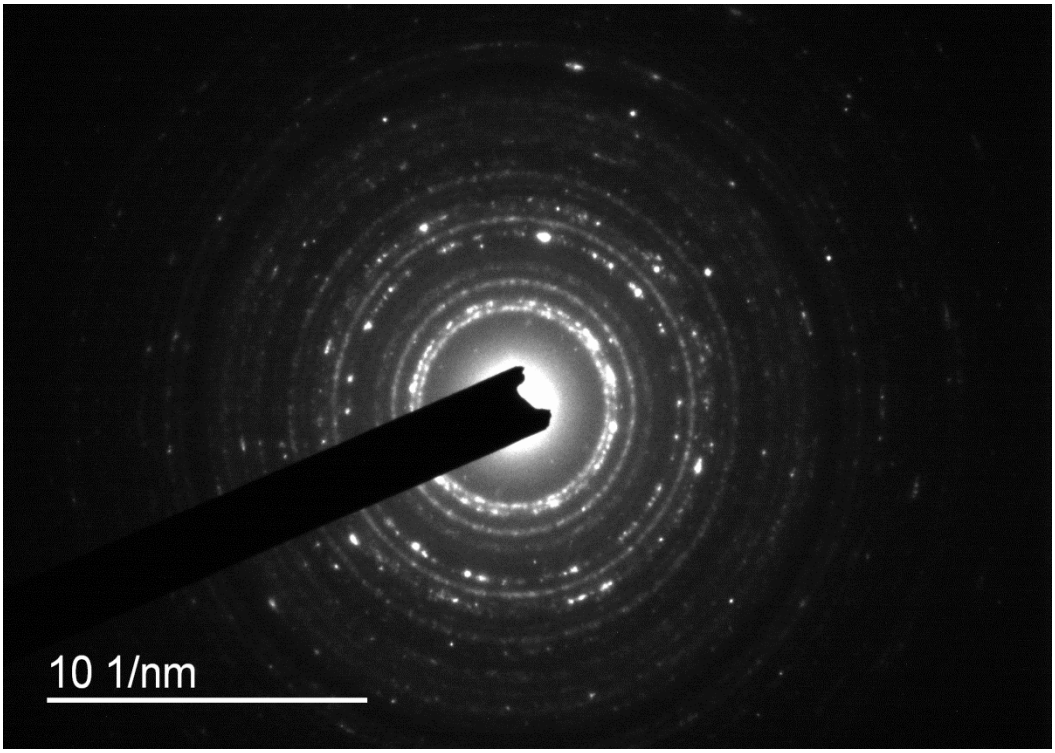

Figure 40.)Selected area electron diffraction image(SAED)

Measurement of individual particle is obvious. When the nanoparticles are bounded together with irregular shape, the accurate size is complex. Tackleing with nanoparticles bounded together, the necking between is examined to find out potentially individual nanoparticles. The diameter of the irregular shaped were measured in fix angle for all particles in the image. As the orientation of the nanoparticles are random, the statistics represents the standard deviation of the samples as shown in Fig 36-37. The size distribution of the nanoparticles obtained from the hydrothermal processing were from 4nm to 11nm. HRTEM images Fig.39 showed the crystallites with the lattice spacing of 3.1Å corresponding to (112) plane of kesterite, and is also of 10nm.

Chapter 5 Optical and electrical properties of ZnO and CZTS based solar cell

5.1 Optical properties of ZnO nanorods

5.1.1 Photoluminescence of ZnO nanorods

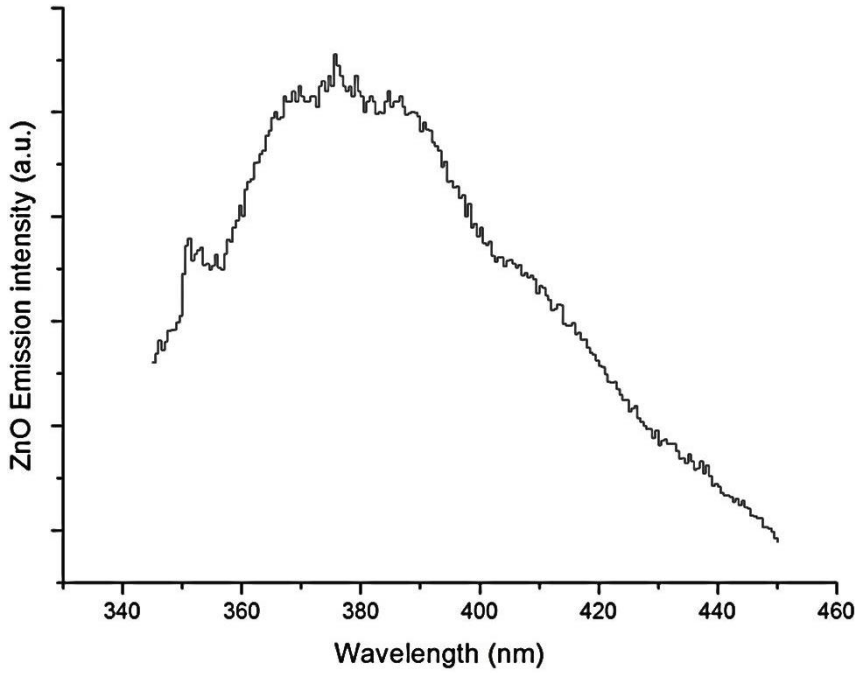

Figure 41.)Photoluminescence emission test of ZnO

On the basis of photoluminescence measurement, the band gap of CZTS was estimated by using a calculation of E=hf in which h is the Planck constan taken as 6.626×10^{-34} , f is the frequency and E is the band-to-band transition energy. Figure 41 shows the PL spectrum of ZnO nanorods, there is a sharp peak found in 380nm, which is corresponding to the emission peak provided. From the emission intensity of the

ZnO, the highest intensity range is from 370nm to 390nm corresponding band to an energy between 3.19eV and 3.35eV.

5.1.2 Photoluminescence of CZTS nano particles

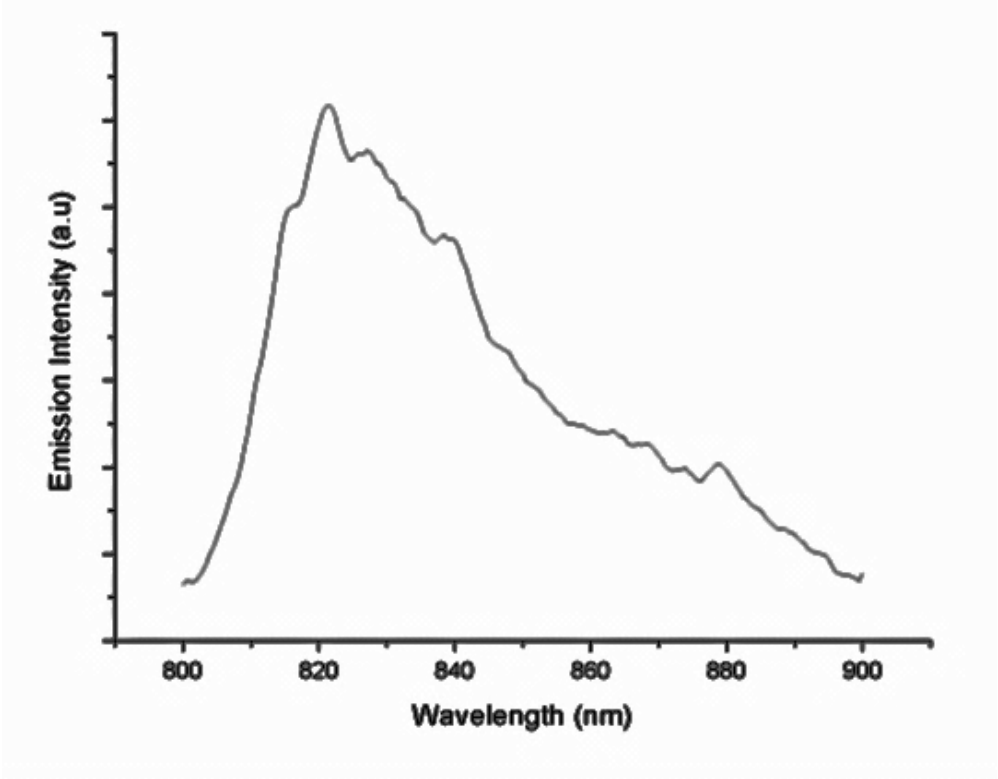

Figure 42.) Photoluminescence emission test of CZTS

On the basis of the photoluminescence measurement, the band gap of CZTS was again estimated. Figure 42 shows the PL spectrum of CZTS nanoparticles. There is a sharp peak found in 820nm, which is corresponding to the band transition emission. From the emission intensity of the CZTS, the highest intensity range is from 810nm to 830nm corresponding to an energy between 1.49eV and 1.53eV.

5.1.3 Ultraviolet-visible spectroscopy of ZnO

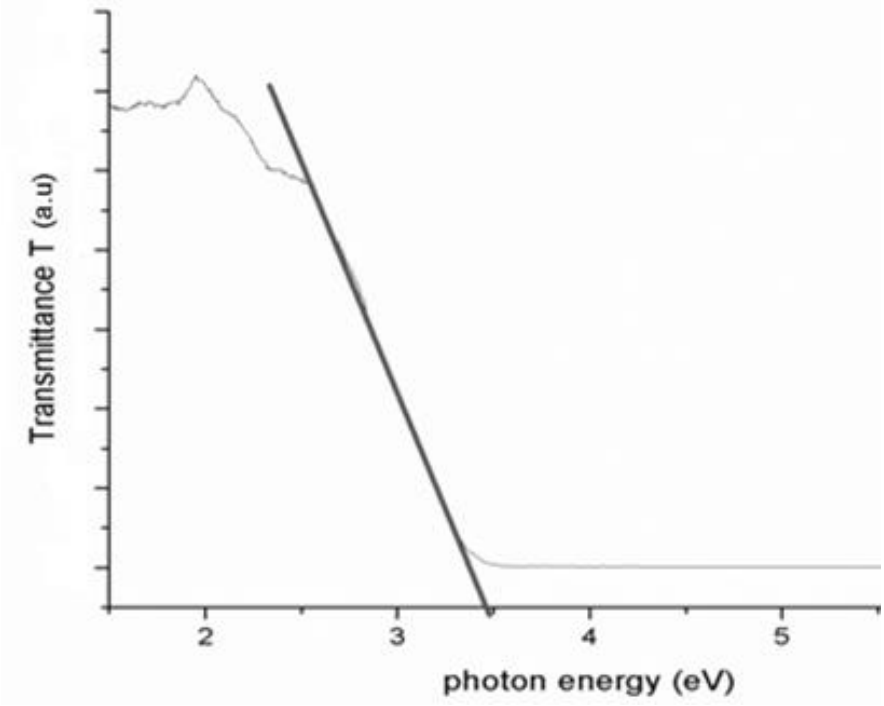

Figure 43.) UV/Vis transmittance versus photon energy spectrum of ZnO

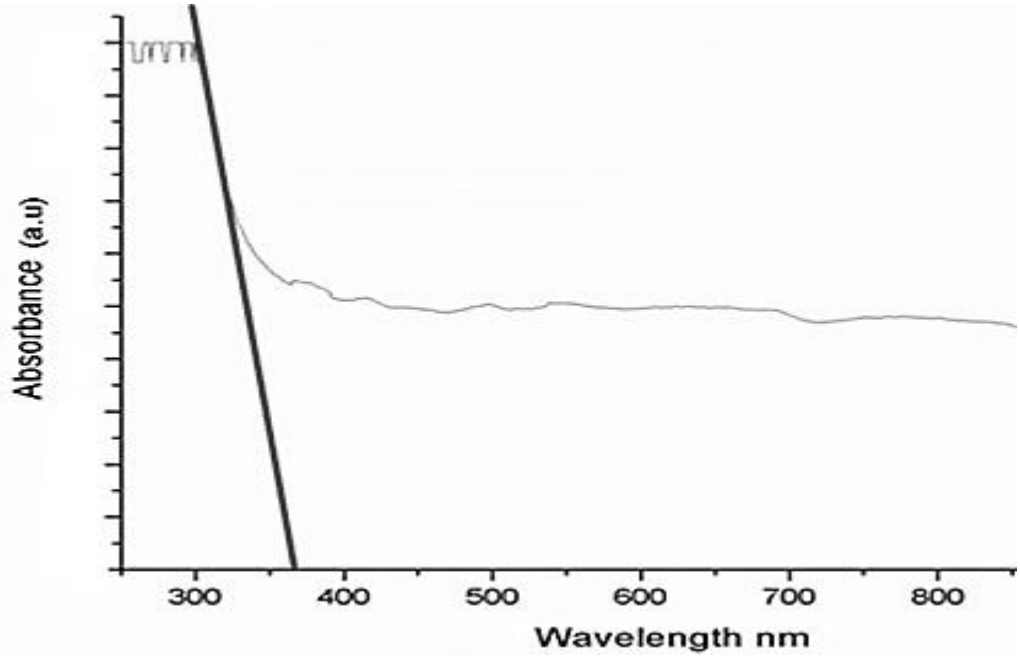

Figure 44.) UV/ Vis absorbance versus wavelength spectrum of ZnO

The ultraviolet-visible spectra of ZnO are shown in figure 43 and figure 44. From the transmittance curve versus photon energy as shown in figure 43, the x-intercept cut is at 3.41eV. At low photon energy, the ZnO was transparent. It is possibly due to the light energy is not sufficient to excite the electrons inside ZnO nanorods. However, when the photon energy continuously increases until it reaches the band gap energy of ZnO nanorods, the electrons inside ZnO valence band receive sufficient energy and are excited to the conduction band. Thus the transmittance of the ZnO nanorods is decreased drastically beyond 3.41eV. This 3.41eV energy gap is consistent with the value obtained in the PL spectrum.

From the absorbance versus wavelength as shown in figure 44, the x-intercept cut is at 368nm. Figure 44 shows high absorbance of ZnO is the decrease with the increase in wavelength. This also means the absorbance of ZnO is increased with the increase in the frequency of source provided. The absorbance of ZnO is increased with the increase in the photon energy. According to E=hf, the higher the frequency of the source the higher is the photon energy. It is possible that, for photon energy lower than the band gap energy of the material, all the light passes through the band gap and not absorbed. When the photon energy reaches or is above the band gap energy of the ZnO nanorods, the electron inside the ZnO nanorod then absorbs the energy from the light source and is excited to certain level. Thus 368nm can be converted to photon energy through E=hf which is found to be 3.38eV. The band gap energy found from absorbance of the ZnO is consistent with the transmittance data.

5.1.4 Ultraviolet- visible spectroscopy of CZTS

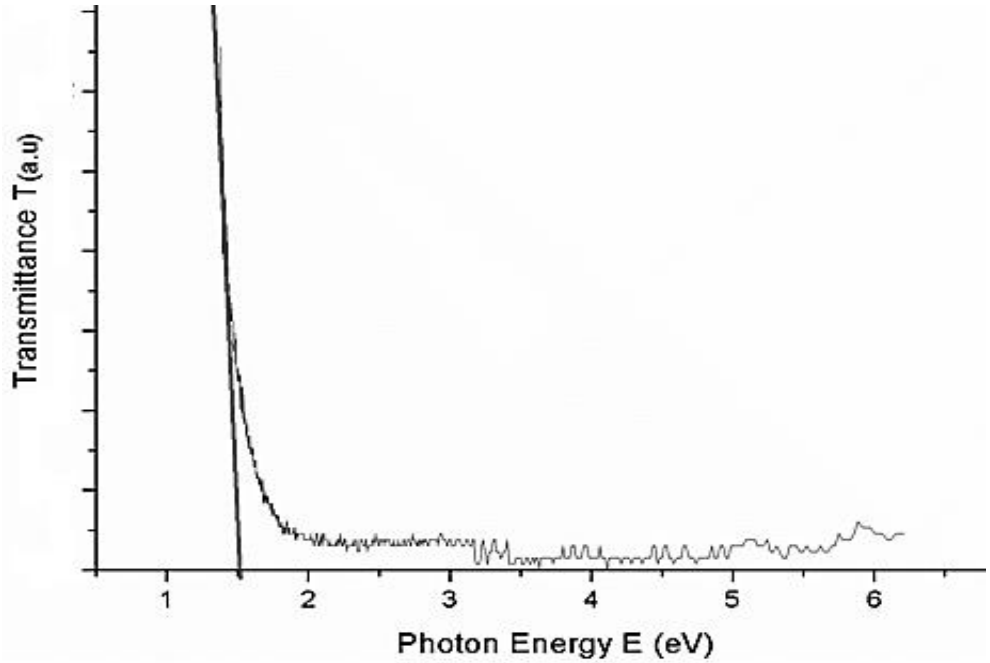

Figure 45.) UV/Vis spectrum of transmittance versus photon energy of CZTS

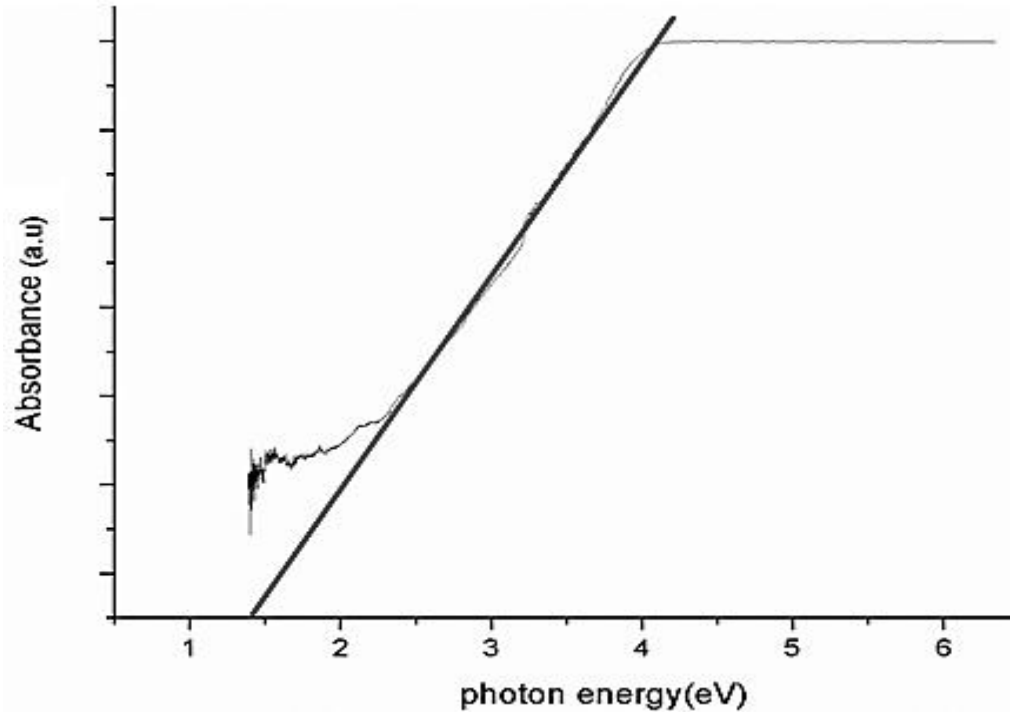

Figure 46.) UV/Vis spectrum of absorption versus photon energy of CZTS

The ultraviolet-visible spectra of CZTS are shown in figure 45 and figure 46. From the transmittance curve versus photon energy as shown in figure 45, the x-intercept cut is at 1.49eV. Low photon energy, the CZTS samples are transparent. It is possibly due to the light energy from the source is not sufficient to excite the electrons inside CZTS nanoparticles. However, when the photon energy continuously increases until it reaches the band gap energy of CZTS nanoparticles, the electrons inside CZTS valence band receive sufficient energy and is excited to the conduction band. Thus the transmittance of the CZTS nanoparitcles is decreased drastically beyond 1.49eV. This 1.49eV energy gap obtained is consistent with that from the PL spectrum.

From the absorption versus photon energy as shown in figure 46, the x-intercept cut is at 1.44eV. Figure 46 shows at very low photon energy, the entire light incident on the samples passes through without absorption. It is possibly due to the energy from the source is not sufficient to excite the electrons inside CZTS nanoparticles. However, when the photon energy continuously increases until it reaches the band gap energy of CZTS nanoparticles, the electrons inside CZTS valence band received sufficient energy and is excited to the conduction band. Thus the absorption of the CZTS nanoparitcles is increased drastically beyond 1.44eV. The data from absorbance curve is also consistent with the PL spectrum.

5.2 Electrical properties

5.1.5 IV characteristics of ZnO nanorods and CZTS nanoparticle based Solar cell

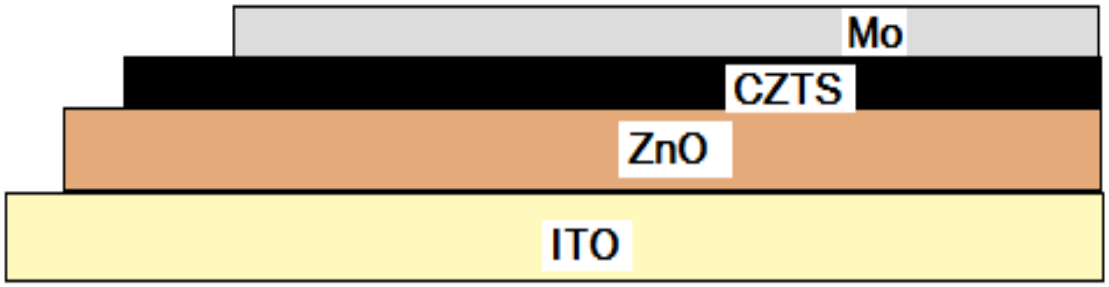

Figure 47.) The layer by layer stacking of the ZnO and CZTS based solar cell

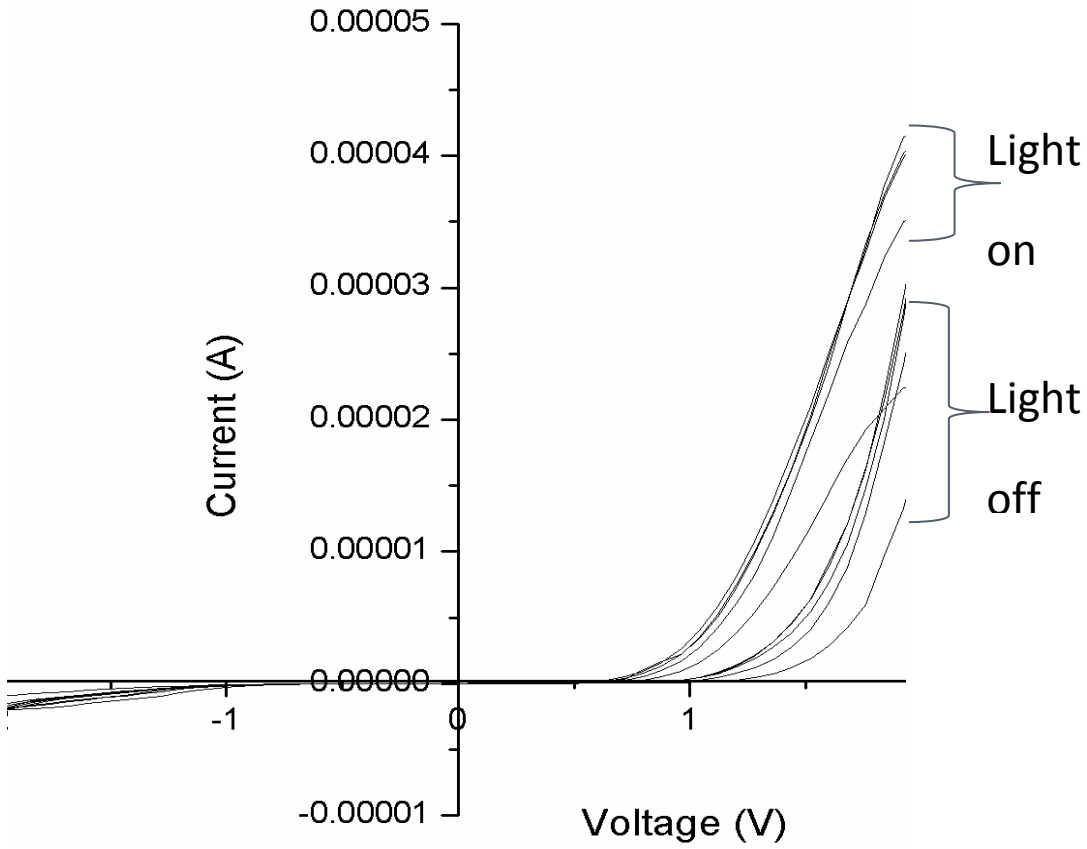

Figure 48.) The current-voltage vurve of the deposited ZnO/CZTS heterojunction

The electrical characteristics of the electrodeposited ZnO/CZTS heterojunctions are shown in figure figure 48. The current-voltage curve shows a typical rectifying profile for this kind of contact in which it is a fundamental profile for recognizing a p-n junction. Since the ZnO shows a n-type conductivity and the CZTS shows a p-type conductivity, the I-V profile obtained is expected to perform a rectifying signal. However, the magnitude of the current response to voltage is very low and down to 10μA~20μA. Figure 48 also shows that the junction also response to the light incident on the samples. The light used in this experiment was a white light emitting diode which simulated the broad wavelength range of light from sun. The build-in potential for the sample shown in figure 48 was estimated to be about 0.8eV.

Figure 47 shows the schematic diagram of the ZnO-CZTS based solar cell fabricated in this thesis. The bottom electrode used was ITO. On top of the bottom electrode, a layer of ZnO nanorod was deposited, acting as the n-type layer. CZTS nanoparticles were coated on to the ZnO layer using drop casting method. The thickness of the ZnO layer and CZTS layer were estimated to be 320 nm and 1μm. On top of this p-n junction, a thick layer of Mo of 400nm sputtered onto the surface, acting as the top electrode. A small increase in current was observed when the junction was indicated by the light source. However, the increase of current during light on is small, only of about 30% increase composed to light off.

Besides, the energy profile for ZnO/CZTS structure is shown is figure 49 which shows the light incident on the ZnO side to the CZTS so that all materials can absorbed and excited the electron hole pairs.

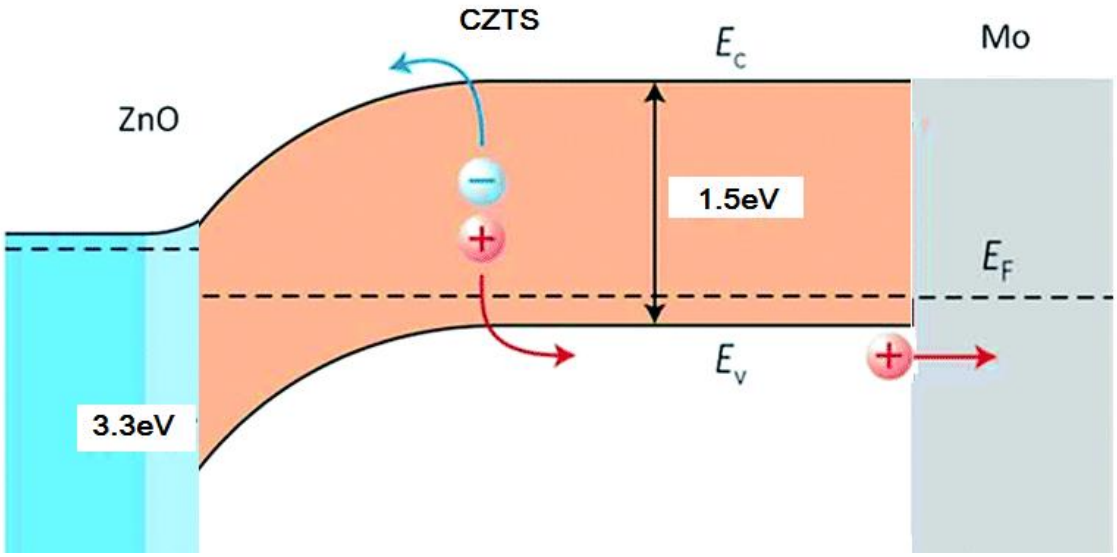

Figure 49.) Electric profile ZnO/CZTS heterojunction solar application

Chapter 6 Conclusion

ZnO thin films have been fabricated successfully through potentiostatic cathodic deposition method. XRD patterns revealed that highly 1 D aligned crystalline films were obtained under most of the fabrication conditions. SEM microstructural studies showed that dense thin film of ZnO with nanorods structure had been obtained. The optimal processing parameters were identified in this project.

Apart from ZnO nanorods, CZTS nanoparticles were successfully fabricated using hydrothermal process at temperature as low as 130^{o}C. Our study revealed that excess amount of Zn and S was necessary in order to fabricated stoichiometric CZTS nanoparticles. By using excess amount of Zn and S, CZTS nanoparticles fabricated were of tetragonal and hexagonal shapes were successfully fabricated.

Besides studying the structural properties, the optical properties of the CZTS and ZnO were also investigated using photoluminescence and UV-Vis spectroscopy. The CZTS nanoparticle was found to have a band gap of value between 1.44eV and 1.49eV. ZnO nanorods were found to have band gap energy of value between 3.35eV and 3.41eV. In order to demonstrate that these two materials can be used as solar cell materials, a prototype ZnO and CZTS solar cell was fabricated. The I-V characteristics of the ZnO-CZTS solar cell were studied. A typical rectifying profile was observed indicating that the ZnO and CZTS formed a p-n junction. Our measurements also indicated that the rectifying profile of the fabricated heterojunction was affected by light, although the charge in the current was not very large.

In order to improve the photovoltaic performance, a detail study should be focus on the deposition of CZTS nanoparticles so that all CZTS nanoparticles will not agglomerate and resulted in low uniformity nanoparticles layer.

References

[1] "Climate Change," [Online]. [Accessed 28 06 2013].

[2] "Climate Change Report," Intergovernmental panel on climate change (IPCC), 2007. [Online]. [Accessed 28 06 2013].

[3] Boden, T.A., G. Marland and R. J. Andres, "Global, Regional, and National Fossil-Fuel Carbon Dioxide Emissions.".*Carbon Information Analysis Center, Oak Ridge National Laboratory, U.S.A.*

[4] C. Geoffrey, "Sunny Uplands: Alternative energy will no longer be alternative," in *The Economist*, 2012-12-28.

[5] Staff writer, "Pricing Sunshine," in *The Economist*, 2012-12-28.

[6] "Reports and publications-Going for grid parity," BP Global, 19 01 2011. [Online].

[7] "Reports and publications- Gaining on the grid parity," BP Global, 19 01 2011. [Online].

[8] Sam Bakdwin, "Energy Efficiency & Renewable Energy: Challenges and Opportunities," *Clean Energy SuperClister Expo Colorado State University. U.S, Department of Energy.,* 2011-04-20.

[9] N. Gupta, G.F.Alapatt, R. Podila, R. Singh and K.F. Poole, "Prospects of Nanostructure-Based Solar Cells for Manufacturing Future Generations of Photovoltaic Modules," *International Journal of Photoenergy,* 2009.

[10] Kallman, H. 且 Pope, M.J., *Chem. Phys.,* 第 冊 30, p. 385, 1959.

[11] Tollin, G., Kearns, D. R. and Calvin, M. J., *Chem. Phys.,* vol. 32, pp. 1013-1019, 1960.

[12] Fox, D., Labes, M. M. and Weissberger, A., *Physics and Chemistry of the Organic SOlid State; Interscience: New York ,* vol. 1, 1963.

[13] Fahrenbruch,A.L and Bube, R.H, "Fundamentals of Solar Cells. Photovoltaic Solar Energy Conversion," *Academic Press,* 1983.

[14] Yu, G., Gao, J., Hummelen, J.C., Wudl, F. and Heeger, A.J., *Science,* 1995.

[15] Hall, J. J. M., Walsh, C. A., Greenhan, N. C., Marseglia, E. A., Friend, R. H., Moratti, S. C. and Holmes, A. B., *Nature,* vol. 376, pp. 498-500, 1995.

[16] Hagfeldt, A. and Gratzel, M. Acc., *Chem. Res.,* vol. 33, pp. 269-277, 2000.

[17] O' Regan, B. and Gratzel, M., *Nature,* vol. 353, pp. 737-740, 1991.

[18] Alfred Smee, "Elements of electro-biology; or the voltaic mechanism of man; of electro-pathology, especially of the nervous system; and of electro-therapeutics," London, Longman, Brown, Green, and Longmans, 1949, p. 15.

[19] Peumans, P., Bulovic, V. and Forrest, S. R., *Appl. Phys. Lett. ,* vol. 76, pp. 2650-2652, 2000.

[20] Heeger, A. J., *J. Phys. Chem. B,* vol. 105, pp. 8475-8491, 2001.

[21] Shaheen, S. E., Brabec, C. J., Sariciftci, N. S., Paddinger, F. and Fromherz, T., *Appl. Phys. Lett.,* vol. 78, pp. 841-843, 2001.

[22] Granstrom, M., Petritsch, K., Arias, A. C., Lux, A., Andersson, M. R. and Friend, R. H., *Nature,* vol. 395, pp. 257-260, 1998.

[23] Gutman, F. and Lyons, L. E., *Organic Semiconductors, Part A; Kreiger: Malabar, 1981.*

[24] "Photovoltaic Cells- Generating electricity," Image Scientific Instrument . [Online]. [Accessed 27 06 2013].

[25] Law, M, Greene, L. E., Johnson, J. C., Saykally, R. and Yang, P., *Nat. Mater,* vol. 4, p. 455, 2005.

[26] Tian, B., Zheng, X., Kempa, T. J., Fang, Y., Yu, G., Huang, J. and Lieber, C. M., *Nature,* vol. 449, p. 885, 2007.

[27] Zhang, Y., Wang, L. W and Mascarenhas, A., *Nano Lett,* vol. 7, p. 1264, 2007.

[28] Adachi, M., Sakamoto, M., Jiu, J., Ogata, Y. and Isoda, S. , *J. Phys. Chem. B,* vol. 110, p. 15932, 2006.

[29] Meng, S., Ren, J. and Kaxiras, E., *Nano Lett.,* vol. 8, p. 3266, 2008.

[30] Surek, T., "Crystal growth and materials research in photovoltaics: progress and challenges.," *Journal of Crystal Growth,* vol. 275, pp. 292-304, 2005.

[31] Kazmerski, L., "NREL Compilation of best research solar cell efficiencies," *N. R.*

E.L.(NREL), no. Golden Colorado, 2010.

[32] V. V. Kislyuk and O. P. Dimitriev, *J. Nanosci. Nanotechnol,* vol. 8, p. 131, 2008.

[33] E. Galoppini, J. Rochford, H. Chen, G. Saraf, Y. Lu, A. Hagfedt and G. Boschloo, *J. Phys. B,* vol. 110, p. 16159, 2006.

[34] Y. Gao and M. Nagai, *Langmuir,* vol. 90, p. 607, 2006.

[35] C. Levy-Clement, R. Tena-Zaera, M. A. Ryan, A. Katty and G.Hodes, *Adv. Mater,* vol. 17, p. 1512, 2005.

[36] J. B. Baxter and E. S. A ydil, *Sol. En. Mat. Sol. Cells,* vol. 90, p. 607, 2006.

[37] Guo, Q., Kim, S. J., Kar, M., Shafaman, W. N., Birkmire, R. W., Stach, E. A., Agrawal, R. and Hillhouse, H. W., *Nano Lett,* vol. 8, p. 2982, 2008.

[38] Panthani, M. G., Akhavan, V., Goodfellow, B., Schmidtke, J. P., Dunn, L., Dodabalapur, A., Barbara, P. F. and Korgel, B. A,, *J. Am. Chem. Soc,* vol. 130, p. 16770, 2008.

[39] Guo, Q., Agrawal, R. and Hillhouse, H., "H. Rapid synthesis of ternary, binary and multinary chalcogenide nanoparticles," *International Patent Application No. PCT,* no. US2007/069349, 2007.

[40] Katagiri, H., Ishigaki, N., Ishida, T. and Saito, K., *Jpn. J. Appl. Phys., Part 1,* vol. 40, pp. 500-504, 2001.

[41] Kaagiri, H., Sasaguchi, N., Hando, S., Hoshino,S., Ohashi, J. and Yokota, T., *Sol. Energy Mater. Sol Cells,* vol. 49, p. 407, 1997.

[42] Tanaka, K., Moritake, N. and Uchiki, H., *Sol. Energy Mater. Sol. Cells,* vol. 91, p. 1199, 2007.

[43] Chet Steinhagen, Matthew G., Panthani, Vahid Akavan, Brian Goodfellow, Bonil Koo and Brian A. Korgel, *J. Am. Chem. Soc,* vol. 131, p. 12554, 2009.

[44] Guo QJ, Hillhouse H. W. and Agrawal. R., *J. Am. Chem. Soc,* vol. 131, p. 11672, 2009.

[45] Riha SC, Parkinson BA and Prieto AL, *J. Am. Chem. Soc,* vol. 131, p. 12054, 2009.

[46] Danaher, W. J. and L. E. Lyons, "Photoelectrochemical cell with cadmium telluride film," *Nature,* vol. 271, p. 139, 1978.

[47] Fulop, G. F. and R. M. Taylor, "Electrodeposition of semiconductors," *Annual Review of Materials Science,* vol. 15, pp. 197-210, 1985.

[48] Basol, B. M., "High-Efficiency Electroplated Heterojunction Solar Cell," *Journal of Applied Physics,* vol. 55, pp. 601-603, 1984.

[49] K. e. a. Ramamoorthy, "Development of a novel high optical quality ZnO thin films by PLD for III-V opto-electronic devices," *Current Physics Letters,* vol. 6, pp. 103-108, 2006.

[50] Wu, S. et al., "Improvement in dye-sensitized solar cells with a ZnO-coated titanium oxideelectrode by rf magnetron sputtering.," *Applied Physics Letters,* vol. 92, p. 122106, 2008.

[51] De Vittorio, M. et al., "Nano-island fabrication by electron beam lithography and selective oxidation of Al-rich AlGaAs layers for single electron device apllication.," *Microelectronic Engineering,* Vols. 61-62, pp. 651-656, 2002.

[52] Fragala, M. E., et al.,, "Colloidal lithography and Metal-Organic Chemical Vapor Deposition process integration to fabricate ZnO nanohole arrays.," *Thin Solid Films,* vol. 518, pp. 4484-4488, 2010.

[53] Jin, Z., et al., "High throughput fabrication of transistion-metal-doped epitaxial properties.," *Applied Physics Letters,* vol. 78, pp. 3824-3826, 2001.

[54] Dharmadasa, I.M. and J. Haigh, "Strenths and Advantages of Electrodeposition as a Semiconductor Growth Technique for Applications in Macroelectronic Devices.," *Journal of The Electrochemical Society,* vol. 153, pp. G47-G52, 2006.

[55] Therese, G. H. A. and P. V. Kamath, "Electrochmical Synthesis of Metal Oxides and Hydroxides.," *Chemistry of Materials,* vol. 12, pp. 1195-1204, 2000.

[56] Bunn, C. W., "The lattice-dimensions of zinc oxide," *Proceedings of the Physical Society,* vol. 47, p. 835, 1935.

[57] Ozgur, U., et al., "Acomprehensive review of ZnO materials and devices," *Journal of Applied Physics,* vol. 94, 2005.

[58] Z. Fan and J. G. Lu, *Journal of Nanosci. Nanotechnol.,* vol. 5, p. 1561, 2005.

[59] X. Liu, X. Wu, H. Cao and R. P. H. Chang, *J. Appl. Phys.,* vol. 95, p. 3141, 2004.

[60] T. Gao, Q. Li and T. Wang, *Chem. Mater,* vol. 4, p. 887, 2005.

[61] W.Zheng, F. Gao and Y. Qian, *Adv. Funct. Mater.,* vol. 15, p. 331, 2005.

[62] R. R. Reeber, *J. Appl. Phys,* vol. 37, p. 5063, 1970.

[63] H. S. Qian, S. H. Yu, J. Y. Gong, L.B. Luo and L. L. Wen, *Crystal Growth & Design,* vol. 5, p. 935, 2005.

[64] X. Wu, H. Bai, C. Li, G. Lu and G. Shi, *Chem. Commun.,* p. 1655, 2006.

[65] B. Baruwati, D. K. Kumar and S. V. Manorama, *Sensors and Actuators B,* vol. 119, p. 676, 2006.

[66] A. N. Baranov, C. H. Chang, O. A. Shlyakhtin and G. N. Panin, *Nanotechnology,* vol. 15, p. 1613, 2004.

[67] H. Braekken, C. Jore and Det Norske Videnskabers Skrifter, "The NorwegianScience Scripts NR8," Norway, 1935.

[68] R.B. Heller, J. McGannon and A. H. Weber, *J. Appl. Phys,* vol. 21, p. 1283, 1950.

[69] T. B. Rymeer and G. D. Archard, *Research,* London, 1952.

[70] T. J. Gary, *J. Am. Ceram. Soc.,* vol. 37, p. 534, 1954.

[71] G. P. Mohatny and L. V. Azaroff, *J. Chem Phys,* vol. 35, p. 1268, 1961.

[72] A. A, Khan, *Acta Crystallog., Sect. A: Cryst. Phys., Diffr., Theor. Gen. crystallogr.,* vol. A24, p. 403, 1968.

[73] C. Wadia, A. P. Alivisatos and D. M. Kammen, *Environ. Sci. Technol,* vol. 43, p. 2072, 2009.

[74] A. Feltrin and A. Freundlich, *Renewable Energy,* vol. 33, p. 180, 2008.

[75] C. A, Wolden, J. Kurtin, J. B. Baxter, I. Repins, S. E. Shaheen, J. T. Torvik, A. A. Rockett, V. M. Fthenakis and E. S. Aydil, *J. Vac. Sci. Technol. A,* vol. 29, p. 030801, 2011.

[76] H. Katagiri, *Thin Solid Films,* pp. 480-481, 2005.

[77] H. Katagiri, K. Jimbo, W. S. Maw, K. Oishi, M. Yamazaki, H. Araki and A. Takeuchi, *Thin Solid Films,* vol. 517, p. 2455, 2009.

[78] I. Repins, M. A. Contreras, B. Egaas, C. Dehart, J. Scharf, C. L. Perkins, B. To and R. Noufi, *Prog. Photovoltaics,* vol. 16, p. 235, 2008.

[79] S. Chen, X. G. Gong, A. Walsh and S. H. Wei, *Appl. Phys. Lett,* vol. 94, p. 041903,

2009.

[80] U. D. o. Energy, *Sunshot Initiative,* 2012.

[81] J. J. Scragg, D. M . B. and P. J. Dal, "A 3.2% percent efficient kesterite device from electrodeposited stacked elementtal layers," *Journal of Electroanalytical Chemistry,* vol. 646, pp. 52-59.

[82] C. Zou and E. A, "Facile Synthesis of CZTS Nanocrystals," *CrystEngComm,* vol. 13, p. 3310.

[83] T. K. Todorov, J. Tang, S. Bag, O. Gunawan, T. Gokmen, Y. Zhu and D. B. Mitzi, "Beyond 11% Efficiency: Characteristics of State- of-the-Art CZTS Solar Cells," *Adanced Energy Materials,* 2012.

[84] H. Katagiri, N. Sasaguchi, S. Hando, S. Hosino, J. Ohashi and T. Yokota, *Sol. Energy Mater. Sol. Cells,* vol. 49, p. 407, 1997.

[85] H. Katagiri, K. Jimbo, S. Yamada, T. Kamimura, W. S. Maw, T. Fukano, T. Ito and T. Motohiro, *Appl. Phys. Express,* vol. 1, p. 041201, 2008.

[86] Bernardini, G. P., Borrini. D., Caneschi. A, Benedetto. F. D., Gatteschi. D., Ristrori. S. and Romanelli. M., "EPR and SQUID magnetometry study of CFTS(stannite) and CZTS(kesterite)," *Physics and Chemistry of Minerals,* vol. 27, pp. 453-461, 2000.

[87] R.K. Pandey, S.N.S. and S. Chandra, "Handbook of semiconductor electrodepotiotion," no. New York Marcel Dekker, 1996.

[88] John M. Cowley, *Diffraction Physics,* pp. ISBN 0-444-10791-6, 1975.

[89] P. Scherrer, *Gottinger Nachrichten Gesell.,* vol. 2, p. 98, 1918.

[90] Patterson, A, "The Scherrer Formula for X-Ray Particle Size Determination," *Phys Rev,* vol. 56, pp. 98-982, 1939.

[91] Egerton,R, "Physical principles of electron microscopy," *Springer,* 2005ISBN0387258000.

[92] Yang Yang, Xiaohui Wang, Changku Sun and Longtu Li, "Photoluminescence of ZnO nanorod-TiO2 nanotube hybrid arrays produced by electrodeposition," *J. Appl. Phys,* vol. 105, no. 9, 2009.

[93] Vlad Andrei Antohe, Loik Gence, Sandeep Kumar Srivastava and Luc Piraux,

"Template-free electrodeposition of highly oriented and aspect-ratio controlled ZnO hexagonal columnar arrays," *Nanotechology,* vol. 23, no. 25, 2012.

[94] M. Himmrich and H. Haeuseler, *Spectrochim. Acta, Part A,* vol. 47, p. 993, 1991.

[95] P. A. Femandes, P. M. P. Salome and A.F. daCrunha, *J. Phys. D,* vol. 43, p. 215403, 2010.

[96] Kallman, H. and Pope, M.J., *Chem. Phys.,* vol. 30, p. 385, 1959.